Power Spectral Density Background Estimate and Signal Detection via the Multitaper Method.

S. Di Matteo[1,2], N. M. Viall[2], L. Kepko[2]

[1]Physics Department, The Catholic University of America, Washington, DC 20664, USA.
[2]NASA - Goddard Space Flight Center, Greenbelt, MD 20771, USA.

Key Points:

- Robust estimate of background power spectrum of time series with parameters uncertainties.
- Our technique combines spectral and harmonic analysis for the identification of periodic fluctuations.
- Methodology includes a modular structure, which allows different smoothing methods and background model options.

Corresponding author: Simone Di Matteo, `simone.dimatteo@nasa.gov`

Abstract

In the spectral analysis of time series, the necessity of a robust determination of the background power spectrum and identification of discrete power enhancements, due to the occurrence of periodic fluctuations, encompasses many research fields. Some application in geophysical and astrophysical observations are the identification of periodic density structures in the solar wind, the distinction between discrete and broadband Ultra Low frequency waves in Earth's magnetospheric field, and the turbulent evolution of the solar wind. Here, we present a new method based on the adaptively weighted multitaper estimate of the power spectral density. Given the direct spectrum (*raw*) and its four different smoothed versions (*med, mlog, bin, but*), we obtain, via a maximum likelihood approach, robust background spectrum estimates according to four models (*WHT, PL, AR(1), BPL*). We select the best representation through statistical criteria and define the confidence levels of possible power spectrum enhancements. We identify periodicities in the time series by combining the discrete power enhancements identified in the spectrum with those identified in the multitaper harmonic F test. We demonstrate the algorithm on a case study of magnetospheric field fluctuations directly driven by periodic structures in the solar wind proton density. The method is robust and flexible, allowing for the characterization of the background spectrum in three distinct environments: the solar wind, magnetosphere, and ground observatories. Using our algorithm to identify background spectra and identify discrete periodicities, we show that there is a directly driven periodicity at $f \approx 0.9$ mHz and possibly at $f \approx 0.2$ and ≈ 0.4 mHz.

1 Introduction.

In the analysis of space physics time series, the distinction between quasi-periodic fluctuations due to underlying physical processes and fluctuations from noise is a challenging task. Identifying periodicities is important in many circumstances, for example the acceleration and loss of radiation belt electrons via ULF wave-particle interactions not only depend on the mode structure of the wave and the azimuthal wave number but also on whether the wave is discrete (drift bounce or drift resonances; Zong et al., 2007; Claudepierre et al., 2013; I. R. Mann et al., 2013) or broadband (radial diffusion; Ozeke et al., 2014). Therefore, the distinction between discrete ULF wave power from broadband wave power is fundamental to address the relative importance of resonant versus stochastic ULF wave interactions. Another example is the analysis of coronagraph im-

ages showing that mesoscale solar wind density structures are periodically released from the top of helmet streamers on time scales of many hours down to the resolutions of the imagers (many minutes; Sheeley et al., 1997; Wang et al., 2000; Viall et al., 2010; Sanchez-Diaz et al., 2017; DeForest et al., 2018) with ≈90 min being one characteristic time scale (Viall & Vourlidas, 2015). In situ measurements of periodic density oscillations showed the presence of these structures between 0.3 and 0.6 AU (Di Matteo et al., 2019) as well as at 1 AU (Viall et al., 2008; Rouillard et al., 2011). Concurrent periodic changes in composition of heavy abundances link the formation of the periodicities with the origin of solar wind parcels from different region of the solar corona (Kepko et al., 2016; Viall et al., 2009). However, Kolmogorov-like power spectra, often observed by several spacecrafts in solar wind magnetic field and velocity measurements, suggested the turbulent expansion of the solar wind (Kolmogorov, 1941; Tu & Marsch, 1995; Bruno & Carbone, 2013; Tsurutani et al., 2018). Therefore, the distinction between periodic fluctuations and the underlying power spectrum is one way to understand the differences between the structured and turbulent nature of the solar wind.

While harmonic analysis to identify the occurrence of periodic variations compared to a flat power spectrum (i.e. white noise) are well established (Fisher, 1929; Percival and Walden, 1993), there is a lack of standard techniques to assess the significance of a periodicity against a colored noise, such as the red spectra typically found in astrophysical and geophysical time series. One of the major diagnostic tools for the identification of quasi-periodic fluctuations in a time series is the frequency domain characterization via the spectral density function $S(f)$, which establishes the distribution of the signal power at specific frequencies. Given a discrete time series $\{x_n\}$ of N data points ($n = 0, 1, \ldots, N-1$) with a sampling rate Δt, the simplest estimator of $S(f)$ is the periodogram based on the time series discrete Fourier transform defined as:

$$X_j = \sum_{n=0}^{N-1} x_n e^{-i2\pi f_j n \Delta t} \qquad \begin{array}{ll} even\, N & j = -N/2, \ldots, N/2 \\ odd\, N & j = -(N-1)/2, \ldots, (N-1)/2 \end{array} \tag{1}$$

where $f_j = j/(N\Delta t)$ are the Fourier frequencies defined over the frequency interval $[-f_{Ny}, f_{Ny}]$, limited by the Nyquist frequency $f_{Ny} = 1/(2\Delta t)$, with the frequency resolution determined by the Rayleigh frequency $f_{Ray} = 1/(N\Delta t)$. The periodogram is defined as the product of the time series sampling rate over the number of points and discrete Fourier transform square modulus: $S_j^{(p)} = (\Delta t/N)|X_j|^2$. The major issues of this estimator are (Percival & Walden, 1993): (i) the leakage of power into adjacent bins, due to the finite

frequency resolution, (ii) a bias in the estimate not known a priori, depending on the time series itself, and (iii) the associated variance, that is equal to the estimate $S_j^{(p)}$ itself. These effects can be reduced by tapering the time series with appropriate weights w_n, satisfying $\sum_n w_n^2 = 1$, and/or by averaging the $S_j^{(p)}$ over adjacent frequency bins (Percival & Walden, 1993). Another procedure consists of averaging the spectral density functions estimated on different weighted subintervals (possibly overlapped) of the original time series (Welch, 1967); since the intervals are shorter, the frequency resolution is reduced. Additionally, many other parametric and non-parametric spectral analysis procedure exist, e.g. minimum prediction error (Samson, 1983), multitaper windowing (Thomson, 1982), and maximum entropy (Vellante & Villante, 1984) method. For real-valued processes, the spectral density function is two-sided, i.e. symmetric about the zero frequency $S(-f) = S(f)$. In this case a common representation is the one sided spectral density function defined as:

$$P(f) = \begin{cases} 0 & f < 0 \\ S(f) & f = 0, f_{Ny} \\ 2S(f) & 0 < f < f_{Ny} \end{cases} \tag{2}$$

often referred as power spectral density or power spectrum. Via the periodogram $S_j^{(p)}$, a simple estimator $P_j^{(p)}$ can be defined on n_f Fourier frequencies f_j with $j = 0, 1, \ldots, (n_f - 1)$. Note that $n_f = N/2 + 1$ for even N and $n_f = (N + 1)/2$ for odd N.

Purely periodic or quasi-periodic signals manifest in the power spectrum as enhancements relative to the continuous background spectrum, i.e. the spectrum due to noise. The identification of the continuous part of the spectrum constitutes a great challenge since sharp peaks can be created by completely different processes, like random/stochastic processes with signals or deterministic chaotic systems (Kantz & Schreiber, 2003). Vaughan (2010) addressed this issue by analysing the occurrence of quasi-periodic oscillations in X-ray observations of Seyfert galaxies (Vaughan, 2005). They introduced a significance test for periodicity assuming red noise spectrum with approximately power law or bending power law (McHardy et al., 2004) shape. Using the statistical properties of the periodogram, Vaughan (2010) applied Markov Chain Monte Carlo techniques to estimate the posterior distribution of the spectrum model parameters. After selecting the best representation of the background spectrum via the sum of the squared standard errors (χ^2) and the likelihood ratio test (Vaughan, 2010; Vaughan et al., 2011), periodic signals manifest as periodogram outliers.

More recently, Inglis et al. (2015) adapted the Vaughan (2010) method to the identification of quasi-periodic pulsations typically observed during the impulsive phase of solar and stellar flares over a wide range of wavelengths. From radio waves and microwaves to hard X-rays and gamma-rays (Nakariakov & Melnikov, 2009), the characteristic timescales of these fluctuations range from one second up to several minutes. The Automated Flare Inference of Oscillations (AFINO; Inglis et al., 2015, 2016) technique probes the power spectrum of the time series for a single power-law-plus-constant model, a broken-power law model, and power-law-plus-constant combined with a Gaussian component in log-frequency space, representing the excess power due to the occurrence of a periodic oscillation. The most appropriate background model is selected via the Bayesian information criterion (Burnham & Anderson, 2004) and a modified χ^2 statistic for exponentially distributed data (Nita et al., 2014). The AFINO technique has been applied also to Flux Gate Magnetometer data from the Magnetospheric Multiscale mission to study the role of the Ultra Low frequency (ULF) waves in the dynamics of the inner magnetosphere and outer radiation belt (Murphy et al., 2018).

M. E. Mann and Lees (1996) proposed another procedure for the distinction between background and peaks in power spectra, based on the spectral and harmonic analyses of Thomson (1982). Briefly, the background spectrum is estimated fitting a lag-one autoregressive model to the median smoothed power spectrum of the time series. Then, a periodicity is identified at locations where the power spectrum enhancements above a confidence threshold are concurrent with harmonic F (HF) test values above a confidence threshold (Thomson, 1982). This method has been applied to many studies of remote and in situ observation of the solar wind.

Here, we combine and improve all of these approaches. Following a brief description of the spectral and harmonic analysis via the multitaper method, we discuss the extension of the maximum likelihood approach, developed for the periodogram, to the multitaper estimates of the power spectrum. Then we introduce various spectrum smoothing approaches to improve the identification of the background spectrum obtained by fitting multiple models. Once the best representation of the background is obtained according to robust criteria, periodic fluctuations manifest as concurrent confident enhancements in the spectral and harmonic analyses.

2 The Multitaper Method

Among the many parametric and non-parametric methods introduced to provide a better estimator of the power spectrum, the Multitaper Method (MTM) is of particular interest (Thomson, 1982), and the one we use in our algorithm. Starting from the spectral representation of a time series $\{x_n\}$ (Cramér, 1940; Koopmans, 1974; Thomson, 1982) with the addition of the phase factor $e^{i2\pi f(N-1)/2}$

$$x_n = \Delta t \int_{-\frac{1}{2\Delta t}}^{\frac{1}{2\Delta t}} e^{i2\pi f\left[n-\frac{N-1}{2}\right]\Delta t} dZ(f) \tag{3}$$

where $dZ(f)$ is an increments process (Cramér, 1992; Percival & Walden, 1993), the corresponding Fourier transform yield the fundamental equation of spectral analysis:

$$y(f) = \sum_{n=0}^{N-1} e^{-i2\pi f\left[n-\frac{N-1}{2}\right]\Delta t} x_n = \Delta t \int_{-\frac{1}{2\Delta t}}^{\frac{1}{2\Delta t}} \frac{\sin\left[N\pi(f-f')\Delta t\right]}{\sin\left[\pi(f-f')\Delta t\right]} dZ(f') \tag{4}$$

It is possible to evaluate an approximate solution for (4) considering the eigenfunctions of the Dirichlet kernel, namely the Slepian functions $U_k(N, W; f)$, that are orthonormal on the interval $[-1/(2\Delta t), 1/(2\Delta t)]$ and orthogonal on $[-W/\Delta t, W/\Delta t]$ with $0 < 2W < 1$ (Slepian, 1978). They are also called discrete prolate spheroidal wave functions and their eigenvalues λ_k represent the fraction of energy in the frequency band $[-W/\Delta t, W/\Delta t]$. The terms of the expansion of $y(f)$ over the interval $(f - W/\Delta t, f + W/\Delta t)$ are called eigencoefficients ($y_k(f)$; Thomson, 1982) and can be evaluated directly from the original time series x_n using the Slepian sequences, namely the discrete prolate spheroidal sequences (DPSS), as data weights before performing the Fourier transform. Ordering the DPSSs with the corresponding eigenvalues in decreasing order, the first $K \leq 2NW - 1$ eigensequences have λ_k close to 1 (Slepian, 1978) and provide, in the case of a white noise process, unbiased and uncorrelated estimates of the spectral density function at the Fourier frequencies f_j (Thomson, 1982): $S_{k,j}^{(mt)} = \Delta t |y_k(f_j)|^2$. For colored spectrum slowly varying over intervals $[f - W/\Delta t, f + W/\Delta t]$, a refined estimator is the adaptive multitaper:

$$S_j^{(amt)} = \frac{\sum_{k=0}^{K-1} d_{k,j}^2 S_{k,j}^{(mt)}}{\sum_{k=0}^{K-1} d_{k,j}^2} \tag{5}$$

in which the weights $d_{k,j}$ are derived from:

$$d_k(f) = \frac{\sqrt{\lambda_k} S(f)}{\lambda_k S(f) + (1 - \lambda_k)\sigma^2} \tag{6}$$

where σ^2 is the variance of the time series. The weights are obtained at the Fourier frequencies f_j by recursively substituting the true spectrum $S(f)$ with the one estimated

by (5). In particular, starting from the average of the spectral estimates $S_{k,j}^{(mt)}$ via the first two DPSSs, we obtain a set of weights from (6), that, when substituted into (5) gives a new estimate of the spectrum to be used for the evaluation of $d_{k,j} = d_k(f_j)$. This procedure reduces the average broad band bias, i.e. the amount of leakage outside a $[f - W/\Delta t, f + W/\Delta t]$ frequency band through the spectrum (Thomson, 1982; Percival & Walden, 1993). As for the periodogram, the power spectral density estimator $P_j^{(amt)}$ can be defined on n_f Fourier frequencies f_j with $j = 0, 1, \ldots, (n_f - 1)$ following eq.(2).

A powerful tool that we use in conjunction with the MTM spectral analysis is the HF test. Starting from the assumption that a time series x_n can be expressed as a superposition of phase coherent harmonic components and a background process ξ_n with a continuous spectrum $S_\xi(f)$ (Thomson, 1982; Ghil et al., 2002), we consider a single signal with constant amplitude A and phase φ at frequency f_0:

$$x_n = \mu(f_0)e^{i2\pi f_0 n\Delta t} + \mu^*(f_0)e^{-i2\pi f_0 n\Delta t} + \xi_n \tag{7}$$

where $\mu(f_0) = \left(Ae^{i\varphi}\right)/2$ and the asterisk denotes the complex conjugation. The evaluation of the corresponding eigencoefficients through the MTM yields a complex-valued regression model (Thomson, 1982; Di Matteo & Villante, 2017) from which an estimate of the amplitude is

$$\hat{\mu}(f_0) = \frac{\sum_{k=0}^{K-1} U_k(N, W; 0) y_k(f_0)}{\sum_{k=0}^{K-1} U_k^2(N, W; 0)} \tag{8}$$

and a statistical confidence interval is given by the HF test

$$F_{2,2K-2}(f_0) = \frac{\chi_2^2}{2} \Big/ \frac{\chi_{2K-2}^2}{2K-2} = \frac{(K-1)|\hat{\mu}(f_0)|^2 \sum_{k=0}^{K-1} U_k^2(N, W; 0)}{\sum_{k=0}^{K-1} |y_k(f_0) - \hat{\mu}(f_0) U_k(N, W; 0)|^2} \tag{9}$$

according to a Fisher distribution. If the initial assumption is not valid and the background spectrum is not locally white or it is related to a chaotic system, spurious lines will be identified at arbitrary frequencies even with high confidence levels. This is the reason why M. E. Mann and Lees (1996) introduced an additional test on the power spectrum. They considered only confident lines in the HF test concurrent with power spectrum enhancements with respect to a background spectrum evaluated fitting a lag-one autoregressive process AR(1) on the convolution of the adaptive multitaper spectrum with a median smoother. In the following section, we extend this approach considering different smoothing procedures of the original spectrum estimate and other background models, fitted via an appropriate maximum likelihood approach.

3 Maximum Likelihood and Confidence Bounds

While fitting a model to an estimated spectrum, we have to consider the probability density function (PDF) of these estimates since they are not gaussian distributed. The periodogram estimates follow an exponential distribution $P_j^{(p)} \sim exp(1/B_j)$ where $B_j = B(f_j)$ is the background spectrum (the expectation value of the periodogram) at the Fourier frequencies $f_{j\neq 0}$ (Anderson et al., 1990; Bevington & Robinson, 2003; Vaughan, 2005). The adaptive MTM estimates instead are represented by a gamma distribution $P_j^{(amt)} \sim Gamma(\alpha_j, B_j/\alpha_j)$ (Thomson & Haley, 2014), where α_j is related at each Fourier frequency to the number of degrees of freedom ν_j defined as (Percival & Walden, 1993)

$$\nu_j = 2\alpha_j = \frac{2\left(\sum_{k=0}^{K-1} d_k^2(f_j)\right)^2}{\sum_{k=0}^{K-1} d_k^4(f_j)} \tag{10}$$

where $d_k(f_j)$ are the final weights obtained from eq.(6).

Considering a model for the background spectrum $B_j(\theta)$ determined by n_θ free parameters $\theta = [\theta_1, \theta_2, \ldots, \theta_{n_\theta}]$, we can proceed with a robust maximum likelihood fitting procedure based on the joint probability density of observing $N/2-1$ power spectral density estimates:

$$L(\theta) = \prod_{j=1}^{N/2-1} p(P_j) \qquad M(\theta) = -2\ln L(\theta) \tag{11}$$

We extend this approach, already adopted for periodograms (Vaughan, 2005, 2010; Vaughan et al., 2011), to MTM spectra. Table 1 summarizes the type of random variable, the probability density function, and the log-likelihood for the periodogram and MTM estimates. Note that the two approaches match each other for $\alpha_j = 1$ corresponding to one direct spectrum estimate ($S_{k,j}^{(mt)}$) among the ones obtained from the different tapered data instances.

Once the background spectrum has been estimated, we probe the occurrence of periodic or quasi-periodic fluctuations searching for enhancements in the power spectral density. In order to distinguish between real power peaks from the stochastic fluctuations due to the random nature of the spectrum estimates, we need confidence thresholds. In previous work, the ratio between the estimated spectrum and the modeled background, often referred as γ, is probed for confidence bounds according to the corresponding probability distribution function (e.g. for the periodogram, $\gamma \sim \chi_2^2/2$). In our case,

Table 1. Probability density function $p(P_j)$ and log-likelihood $M(\theta)$ of the power spectral density P_j estimated via the periodogram and the MTM at the Fourier frequencies f_j.

Periodogram: $P_j = P_j^{(p)}$	Multitaper Method (MTM): $P_j = P_j^{(amt)}$
$P_j = B_j \frac{\chi^2_2}{2} \sim exp\left(\frac{1}{B_j}\right)$	$P_j = B_j \frac{\chi^2_{2\alpha_j}}{2\alpha_j} \sim Gamma\left(\alpha_j, \frac{B_j}{\alpha_j}\right)$
$p(P_j) = \frac{1}{B_j} e^{-P_j/B_j}$	$p(P_j) = \frac{\alpha_j}{\Gamma(\alpha_j)B_j}\left(\frac{\alpha_j P_j}{B_j}\right)^{\alpha_j - 1} e^{-\frac{\alpha_j P_j}{B_j}}$
$M(\theta) = 2\sum_j \left[\frac{P_j}{B_j} + \ln(B_j)\right]$	$M(\theta) = 2\sum_j \left[\frac{\alpha_j P_j}{B_j} + \ln\left[\Gamma(\alpha_j)P_j\right] - \alpha_j \ln\left(\frac{\alpha_j P_j}{B_j}\right)\right]$

from table 1, at each Fourier frequency $f_{j\neq 0}$:

$$\gamma_j = \frac{P_j}{B_j} = \frac{\chi^2_{2\alpha_j}}{2\alpha_j} \sim Gamma\left(\alpha_j, \frac{1}{\alpha_j}\right) \tag{12}$$

However, if we consider the ensemble of γ_j as n_f possible representation of a single random variable γ, being n_f the number of frequencies, the corresponding probability distribution function is:

$$p(\gamma) = p(\gamma/\alpha)p(\alpha) \qquad with \quad p(\gamma/\alpha) \sim Gamma(\alpha, \frac{1}{\alpha}) \tag{13}$$

where $p(\alpha)$ is the probability distribution function of the half number of degrees of freedom, that we estimate via a simple histogram of the α_j values over the range $[0, K]$ with a fixed step of $\Delta\alpha = 0.2$. The use of more sophisticated methods for the estimation of $p(\alpha)$, like the nearest neighbour or the kernel methods (Silverman, 1986), are computational expensive and only determine differences lower than the 1.0% on the final confidence level with respect to the simple histogram.

To define the cutting value z, we need the corresponding cumulative distribution function. Considering that $0 < \alpha < K$ by definition and that $z > 0$, since the spectral density function is always positive, we obtain:

$$P(\gamma < z) = \int_0^z p(\gamma')d\gamma' = \int_0^K \frac{\alpha}{\Gamma(\alpha)}\alpha^{\alpha-1}\left(\int_0^z \gamma'^{\alpha-1}e^{-\alpha\gamma'}d\gamma'\right)p(\alpha)d\alpha \tag{14}$$

Introducing the normalized lower incomplete gamma function:

$$P_x(a) = \frac{\int_0^x e^{-t}t^{a-1}dt}{\int_0^\infty e^{-t}t^{a-1}dt} = \frac{\gamma(a,x)}{\Gamma(a)} \tag{15}$$

the cumulative distribution function for the random variable γ is:

$$P(\gamma < z) = C_K(z) = \int_0^K P_{\alpha z}(\alpha)p(\alpha)d\alpha = c \tag{16}$$

249 At a given confidence level c, the cutting value z_c can be evaluated by searching for the
250 zero of the function $g(z) = C_K(z) - c$ estimated via trapezoidal numerical integration.

251 4 Practical Procedure

252 The structure of our procedure is outlined with a flowchart in Figure 1. Given a
253 time series x_n defined on the time steps t_n, we subtract by default the average value $<$
254 $x_n >$. Note that data trends, due to long term variations on the same timescale of the
255 length of the interval, might affect the results. In this case, the user should deal with a
256 prewhitening of the time series if necessary. At this point, an optional step is the zero
257 padding of the data that is a virtual extension of the length of the time interval to re-
258 duce the frequency separation between Fourier frequencies. Once the corresponding Slepian
259 sequences are evaluated, we estimate the adaptive multitaper power spectrum and the
260 Harmonic F values. In the following sections, we carefully describe our new procedure
261 for the characterization of the background spectrum and the identification of signals. First,
262 we list the spectrum smoothing approaches and the implemented background models.
263 Their combination provide a set of possible background spectra among which the best
264 representation is selected according to specific selection criteria. Finally, we discuss the
265 combination of the background spectrum and the HF test for the identification of sig-
266 nals at given confidence levels.

267 4.1 Smoothing.

268 The identification of the background spectrum or noise level can be strongly influ-
269 enced by embedded signals creating large enhancements in the power spectrum. The ma-
270 jor consequence is the introduction of a bias that increases the estimated background
271 level, possibly along the entire frequency range, leading to selection of power peaks at
272 lower confidence levels. The smoothing of the estimated power spectrum is a way to re-
273 duce this effect (Percival & Walden, 1993). In the following we propose four different ap-
274 proaches in which the degree of smoothing is determined by a percentage value p of the
275 frequency interval $[0, f_{Ny}]$.

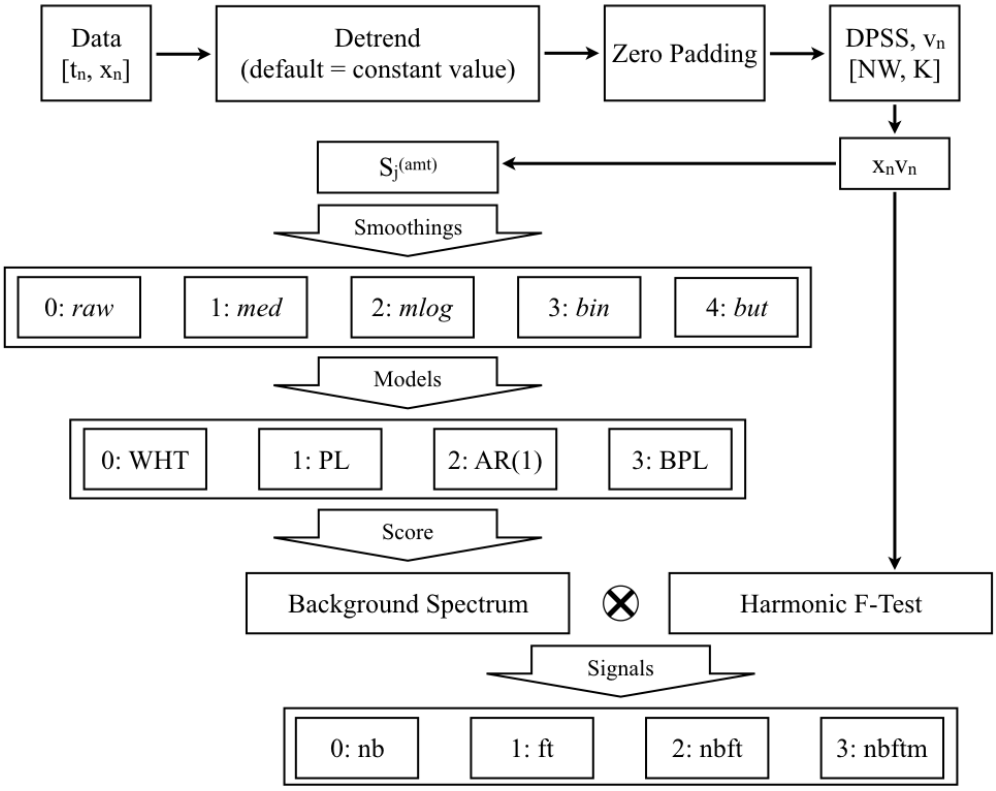

Figure 1. Flowchart outlining the steps of our procedure (see section 4 for details).

4.1.1 Running Median (med).

Given the estimated power spectrum P_j with $j = 0, 1, \ldots, (n_f - 1)$, the smoothing via the running median is performed over frequency intervals of $M = 2w+1$ points.

$$P_{med,j} = median(P_k) \quad with \quad k = j - w, \ldots, j + w \tag{17}$$

Near the edges of the frequency interval the window is truncated to fewer points. The number of points, determined by w, are evaluated from a percentage value p relative to the available frequency interval. For example, given the complete interval $[0, f_{Ny}]$ and the percentage value p (such that $0 < p < 1$), the width of the smoothing window is $M \approx (pf_{Ny})/f_{Ray}$. A useful guideline in the choice of p, suggested by M. E. Mann and Lees (1996), is $NWf_{Ray} \lesssim pf_{Ny} \lesssim f_{Ny}/4$.

4.1.2 Running Median on Uniform Logarithmic Frequency Window (mlog).

When facing colored spectrum with steep variations, the running median does not provide an accurate representation of the spectrum. For geophysical signals, typically

manifesting a red noise nature, the critical range is at low frequencies (M. E. Mann & Lees, 1996). A better approach was suggested by Stella et al. (1994) who proposed a running median on windows with uniform width with respect to the central frequencies in the logarithmic frequency space.

$$P_{mlog,j} = median(P_k) \tag{18}$$
$$with \quad k : |log(f_j) - log(f_k)| \leq psmooth * log(f_{Ny})/2$$

An appropriate choice of the percentage of smoothing p follows the previous guidelines so that $\log(NWf_{Ray}) \lesssim p\log(f_{Ny}) \lesssim \log(f_{Ny}/4)$. Even though the median calculated over a uniform window in logarithmic space includes only a few points at low frequencies, which enables the recovery of the steep nature of the spectrum, it loses accuracy at high frequencies where a large portion of the frequency range is included, leading to a flattening of the smoothed spectrum.

4.1.3 Binned Logarithmic Spectrum (bin).

The running average of the logarithmic power spectrum over $M = 2w + 1$ data points is associated to the geometric mean of the corresponding frequencies.

$$\log\left[P_{bin}(f_{bin,j})\right] = \frac{1}{M}\sum_k \log\left[P_k\right] \qquad and \quad f_{bin,j} = \left(\prod_k f_k\right)^{1/M} \tag{19}$$

with $k = j - w, \ldots, j + w$. At the edges of the frequency interval we fill the missing points mirroring the data. For example, at $j = 0$ with $M = 5$ we would consider $k = [1, 0, 0, 1, 2]$; the same argument is applied at the upper edge. Papadakis and Lawrence (1993) showed that this is an unbiased estimator of the true power spectrum at the set of frequencies $f_{bin,j}$ in the case of power law spectrum. They also remark that the bias is small as long as the logarithm of the spectral density varies smoothly with the logarithm of frequency. As a consequence, the choice of the window M should be such that this condition is valid; as a general guideline we consider the same limits imposed for the running median procedure.

4.1.4 Butterworth Filter (but).

In this option for smoothing, we apply a butterworth low pass filter and smooth the power spectral density as if it were a time series. The butterworth gain function is

given by:

$$G(f') = \frac{1}{\sqrt{1 + \left(\frac{f'}{f_c}\right)^{2n}}} \tag{20}$$

where f' are the "frequencies", f_c is the cutoff frequency, and n is the order of the filter. Usually, after filtering, the smoothed series manifests problems at the boundaries of the interval. To overcame this issue, we first extended the amount of data by introducing before and the after the spectrum a mirrored replicate of itself. Then, we evaluate the Fast Fourier Transform of the signal and multiply it for the butterworth filter's gain function. Finally, the central part of the inverse Fourier transform provides the smoothed power spectrum. Here, the percentage of smoothing p regulates the value of the cutoff frequency $f_c = pf_{Ny}/8$ such that $0 < f_c \leq f_{Ny}/8$, while the order is set to $n = 17$. The choice of this parameters is arbitrary, even though this combination has been proven to provide reasonable results in various synthetic data representation (white and colored noise). For spectrum with steep variations, this procedure manifests issues similar to the ones occurring for the running median.

4.1.5 Adaptive Smoothing: Kolmogorov-Smirnov Test.

The choice of the optimum window for the smoothing procedure can be also based on statistical tests when the probability density function of the spectrum estimates is known. Stella et al. (1994) showed that a Kolmogorov-Smirnov (KS) test, comparing the cumulative distribution function of a random variable to a test function, can be applied to the ratio between the periodogram and its smoothing. In a similar way, for the MTM we can apply the same concept to γ, as defined in eq.(12). The data points can be converted to an unbiased estimator of the cumulative distribution function $C_\gamma(z)$ with $z > 0$ providing the fraction of data points minor than a certain value z. The theoretical cumulative distribution function for the ratio γ is $C_K(z)$ as defined in eq.(16). The KS test (Press et al., 2007) probes the similarity between these two cumulative distribution functions evaluating their maximum distance:

$$D_{KS} = max(|C_\gamma(z) - C_K(z)|) \tag{21}$$

Therefore, the optimal percentage of smoothing (p_{KS}) is the one providing the $C_\gamma(z)$ that minimize the D_{KS} value.

346 ### 4.2 Background Models

347 Once the power spectrum P_j and its different smoothed versions have been eval-
348 uated, we can test the background spectrum for simple parametric models $B_j(\theta)$ rep-
349 resentative of a wide range of variable systems in geophysics. The best parameters $\hat{\theta}$ are
350 determined from the maximum likelihood procedure outlined in section 3.

351 #### *4.2.1 White Noise (WHT).*

352 The simplest background model is the white noise spectrum, where the power is
353 evenly distributed among the Fourier frequencies:

354 $$B_j(\theta) = N \quad \theta = [N] \tag{22}$$

355 The only limit imposed on the parameter is for it to be positive $N > \varepsilon$. The $\varepsilon \gtrsim 0$
356 value is required to avoid the nonphysical result of null spectrum. The initial value N_0
357 (table 2), imposed when maximizing the likelihood, has been derived from the relation
358 between the variance of a stochastic process and the integral of the spectral density func-
359 tion (Percival & Walden, 1993):

360 $$\int_{-f_{Ny}}^{f_{Ny}} S(f)df = \sigma^2 = var\{x_n\} \tag{23}$$

361 Note that the same is valid for the power spectrum $P(f)$ when integrated over the in-
362 terval $[0, f_{Ny}]$. Substituting the white noise parameterization and considering the con-
363 tinuous spectrum, we obtain N_0.

364 #### *4.2.2 Power Law (PL).*

365 Another common representation of the background spectrum is the power law model:

366 $$B_j(\theta) = N f_j^{-\beta} \quad \theta = [N, \beta] \tag{24}$$

367 A rough estimate of β is the slope of the logarithmic spectrum, while for N we use eq.(23)
368 limiting the integration interval to $[\Delta f, f_{Ny}]$ (see table 2).

369 #### *4.2.3 Lag-one Autoregressive (AR(1)).*

370 When considering discrete finite red noise time series, the simplest statistical pro-
371 cess one can assume is the lag-one autoregressive process AR(1) represented by $x_n =$

$\rho x_{n-1} + w_n$. Physically it is reasonable to expect that the present value of a time series x_n depends on the past values x_{n-1} by the degree of serial correlation (the lag-one autocorrelation coefficient $0 \leq \rho < 1$) together with some random effect w_n (white process with variance σ^2). It is representative of many geophysical systems (M. E. Mann & Lees, 1996). The autocorrelation of a AR(1) process decays exponentially with a characteristic time determined by $\tau = -\Delta t / \log(\rho)$, therefore, on time scales larger than τ it behaves as a white process. The corresponding power spectrum is given by (M. E. Mann & Lees, 1996; Vaughan et al., 2011)

$$B_j(\theta) = \frac{N}{1 - 2\rho\cos(\pi\frac{f_j}{f_{Ny}}) + \rho^2} \quad \theta = [N, \rho] \tag{25}$$

Note that for $\rho = 0$ it reduces to a white process. The rough estimates of the model parameters (table 2) are derived for ρ_0 directly from the definition of the AR(1) process, and for N_0 from eq.(23) (see table 2).

4.2.4 Bending Power Law (BPL).

A more flexible approach is the adoption of analytical functions able to reproduce the general behaviour of geophysical signals spectra, even though they are not related to a particular stochastic process. An example is the bending power law defined as (Vaughan et al., 2011)

$$B_j(\theta) = \frac{N f_j^{-\beta}}{1 + \left(\frac{f_j}{f_b}\right)^{\gamma-\beta}} \quad \theta = [N, \beta, \gamma, f_b] \tag{26}$$

There are four parameters: the normalization N, the spectral indices β and γ dominating respectively the frequency intervals below and above the frequency break f_b at which the model bends. This model is particularly helpful when analyzing time series of turbulent systems. In fact, the corresponding power spectrum presents power law trends, with different spectral indices at frequency below and above a frequency break, corresponding to different regimes of the energy cascade. As in the previous model, a rough estimate of the parameters (table 2) is provided assuming the frequency break at the center of the interval in analysis, the spectral indices as the slope of the logarithmic spectrum in the respective frequency range, and the normalization factor from eq.(23).

4.2.5 Confidence Levels of the Models Parameters.

We use the maximum likelihood method for the determination of confidence intervals for the model parameters. Our approach is a modified version of the Likelihood Ra-

Table 2. Models parameters starting values and imposed range[a] for the log-likelihood minimization procedure.

Model	Rough Parameters Estimate	Parameters Range
WHT	$N_0 = \frac{\sigma^2}{f_{Ny}} \approx \frac{1}{n_f - 1} \sum_j P_j$	$\theta_{min} = [\varepsilon]$
$\theta = [N]$		$\theta_{max} = [+\infty]$
PL	$\beta_0 = \log(P_{j'}/P_{j''}) / \log(f_{j''}/f_{j'})$	$\theta_{min} = [\varepsilon, 0]$
$\theta = [N, \beta]$	$N_0 = \sigma^2 / \int_{\Delta f}^{f_{Ny}} f^{-\beta_0} df$	$\theta_{max} = [+\infty, 10]$
AR(1)	$\rho_0 = mean(x_n x_{n-1})/\sigma^2$	$\theta_{min} = [\varepsilon, 0]$
$\theta = [N, \rho]$	$N_0 = \sigma^2 / \int_{\Delta f}^{f_{Ny}} 1/(1 - 2\rho_0 \cos\left(\frac{\pi f}{f_{Ny}}\right) + \rho_0^2) df$	$\theta_{max} = [+\infty, 1]$
	$f_{b0} = f_{j^*} \quad with \quad j^* \approx (j'' - j')/2$	$\theta_{min} = [\varepsilon, 0, 0, \Delta f]$
BPL	$\beta_0 = \log(P_{j'}/P_{j^*}) / \log(f_{j^*}/f_{j'})$	$\theta_{max} = [+\infty, 10, 10, f_{Ny}]$
$\theta = [N, \beta, \gamma, f_b]$	$\gamma_0 = \log(P_{j^*}/P_{j''}) / \log(f_{j''}/f_{j^*})$	
	$N_0 = \sigma^2 / \int_{\Delta f}^{f_{Ny}} f^{-\beta_0} / \left[1 + (f/f_{b0})^{\gamma_0 - \beta_0}\right] df$	no padding: $\Delta f = f_{Ray}$

[a]To avoid the non physical result of null spectrum a lower $\varepsilon \gtrsim 0$ limit is necessary for the normalization factor N.

tio Confidence Bounds (Cash, 1976, 1979; Lampton et al., 1976; Protassov et al., 2002). Once the optimum set of parameters $\hat{\theta}$ has been identified for a specific model, from the relations in table 1 we define the likelihood ratio as

$$L_R(\theta) = \frac{L(\theta)}{L(\hat{\theta})} = \exp\left\{\sum_j \alpha_j \left[\ln\left(\frac{\hat{B_j}}{B_j}\right) + P_j \frac{B_j - \hat{B_j}}{B_j \hat{B_j}}\right]\right\} \tag{27}$$

in which $\hat{B_j}$ is the background spectrum according to the $\hat{\theta}$ parameters and $0 < L_R(\theta) < 1$. Our approach can be divided into four steps. First, we evaluate the likelihood ratio over a coarse grid in the parameters space $\theta \in [\theta_{min}, \theta_{max}]$ and we estimate $\tilde{L}_R = \int_{\theta_{min}}^{\theta_{max}} L_R(\theta) d\theta$ with a numerical rectangular integration. Note that the limits θ_{min} and θ_{max}, defined in table 2, are optimized for red colored spectra, but the entire procedure can be extended to other models as long as these and the θ limits constitute an appropriate choice. Second, we determine a reduced range for the model parameters $\theta' = [\theta'_{min}, \theta'_{max}]$ for which the integrated likelihood ratio $\tilde{L}'_R$ does not vary more than $\varepsilon \tilde{L}_R$ with respect to the original integral, that is $\tilde{L}'_R / \tilde{L}_R \lesssim 1 - \varepsilon$ with $\varepsilon = 10^{-9}$. Third, we define a fine grid over

the parameters range θ' obtaining a better estimate of the integrated likelihood ratio $\tilde{L}'_R$. Finally, the confidence levels for the model parameters are the extrema of the range θ_C over which the integrated likelihood ratio is $C\tilde{L}_R$ with respect to the original integral. For example, we can define the "1σ" intervals imposing a confidence level of ≈68.3% (C=0.683).

4.3 Best Background Spectrum Choosing Criteria.

The combination of the possible smoothing and models creates a variety of background spectral estimates that in some cases are very similar. Here, we introduce three tests based on the stochastic properties of the adaptive MTM spectrum estimates that provides objective criteria to choose the best representation of the background spectrum.

AIC. Based on the likelihood and the number of free parameters n_θ of each model, a useful method of comparison is the the Akaike Information Criterion (AIC) (Akaike, 1973).

$$AIC = -2\ln[L(\theta)] + 2n_\theta \tag{28}$$

It corresponds to the sum of the log-likelihood with a penalty value for including more free parameters. This is a standard tool in maximum likelihood analysis and allow the comparison of non-nested model (Vaughan, 2005). The best background spectra corresponds to the model that minimises the AIC.

MERIT. Anderson et al. (1990) defined a fit acceptable when a $MERIT$ value, defined as the ratio between the weighted sum of squared errors and the number of degrees of freedom (difference between the number of points and the number of the model free parameters), was lower than 1. For the adaptive MTM spectrum, the $MERIT$ value is

$$MERIT = \frac{1}{n_f - n_\theta}\sum_j \frac{(P_j - E\{P_j\})^2}{var\{P_j\}} = \frac{1}{n_f - n_\theta}\sum_j \alpha_j \left(\frac{P_j - B_j}{B_j}\right)^2 \tag{29}$$

where we use the expected value of the variance associated to the adaptive MTM (Thomson & Haley, 2014), that are respectively $E\{P_j\} = B_j$ and $var\{P_j\} = B_j^2/\alpha_j$. This value represents the goodness of fit for least square problems (Bevington & Robinson, 2003), but in our case, since the distribution of our data differ from a Gaussian distribution, it represents only a comparison tool. As for the AIC, the lower is the $MERIT$ value the better is the representation of the background spectrum by the adopted model.

C_{KS}. A Kolmogorov-Smirnov test (described in section 4.1.5) can be applied to the ratio between the adaptive MTM spectrum and the background model (see eq.12). First, we evaluate D_{KS} that is the maximum distance between the empirical and theoretical cumulative distribution functions. Then, for the null hypothesis, that is data belonging to the same distribution, the significance level for D_{KS} can be approximately estimated by (Press et al., 2007):

$$P(D > D_{KS}) = Q_{KS}(\sqrt{n_f} D_{KS}) \quad with \quad Q_{KS}(\lambda) = 2\sum_{j=1}^{\infty}(-1)^{j-1} e^{-2j^2\lambda^2} \tag{30}$$

where n_f is the number of spectrum points tested. Finally, a confidence level for the fit is defined as $C_{KS} = 1 - P(D > D_{KS})$ so that, in a similar way to the previous approaches, the minimum value corresponds to the model that best represent the background spectrum.

In our procedure, we associate each combination of smoothings and models with a *score*, defined as the product of the three tests, namely *score=AIC*MERIT*C_{KS}*. The best representation of the background spectrum corresponds to the smoothing+model pair that minimizes the *score*. When there are very strong enhancements in the spectrum, showing clear deviation from the surrounding spectrum, the *score* struggles in providing a reasonable answer. Discrete power enhancements are not parameterized in the implemented models, therefore, the distribution of the γ values deviate from the theoretical one at the peak position. Smoothing procedures reduce this effect, but better results can be obtained removing the portion of the power spectrum estimates above the 99.99% confidence level ($z_{99.99\%}$) as defined by eq. (16), see section 4.4 for more details.

4.4 Selection of Power Spectrum Enhancements.

Once the background spectrum has been identified, we can search for the occurrence of power spectrum enhancements related to the presence of periodic fluctuations in the time series. First, we consider every portion of the power spectrum above a threshold defined as the product of the background spectrum and the cutting value z_c obtained by eq. (12), corresponding to the confidence level c. Then, we perform a narrow band test selecting only the peaks whose width is at least greater than W, the halfbandwidth of the MTM spectral window. In the MTM approach, spurious peaks exhibit a triangular shape (the width decreases for higher confidence levels) while enhancements due to real periodicity manifest a rectangular shape of width $\approx 2W$ (Thomson & Haley, 2014).

Due to the distortion of the enhancements shape caused by noise (especially for low signal to noise ratio) we set a lower limit of W on the width. No upper limit is imposed to include also the broad enhancements possibly related to the occurrence of multiple signals at close frequencies (Di Matteo & Villante, 2017). For each portion of the spectrum that passes the test, we identify the central frequency and the half width (narrowband approach, *nb*). An independent test for the selection of signals is the HF test as described in section 2. In this case, we select all the local maxima values above the confidence level obtained by the Fisher distribution (F test approach, *ft*). We combine the results of the two tests in the last option. In this case, the selected frequencies are the ones identified in the HF test that are within the narrowband spectrum enhancement (narrowband + F test approach, *nbft*). Finally, for the last choice, we impose the more stringent criterion and allow only one signal for each narrow band, corresponding to the maximum value obtained from the HF test (narrowband + maximum F test approach, *nbftm*).

5 Examples with Synthetic Data.

We demonstrate the steps of our procedure below using synthetic time series representing lag-one autoregressive, power law, and bending power law processes. There are many methods to generate synthetic data with a specific power spectrum shape (Anderson et al., 1990; Timmer & Koenig, 1995; Vaughan et al., 2011). For an AR(1) process we use its definition as stated in section 4.2: given a random starting point x_0 and the lag-one autocorrelation coefficient ρ, the values of the time series for the following steps are $x_{n+1} = \rho x_n + w_n$ in which w_n is a Gaussian distributed random number (with zero mean and unitary variance). For the power law and bending power law processes, we use the approach of Timmer and Koenig (1995). Briefly, the square root of half the power spectrum is multiplied for two different series of Gaussian distributed random numbers. These vectors are extended with their complex conjugate to retrieve the real and imaginary part of the double-sided Fourier transform of the desired data, so that the synthetic data are obtained as its inverse Fourier transform. Starting from the same white noise time series, we generate three synthetic processes representation of N=360 points with sampling rate $\Delta t = 60s$, unitary variance, and parameters representative of the solar wind/magnetosphere environment: i) $N = 25.5[(a.u.)^2/Hz]$ and $\rho = 0.90$ for the AR(1); ii) $N = 8.92{\times}10^{-4}[(a.u.)^2/Hz^{1-\beta}]$ and $\beta = 5/3$ for the power law; iii) $N = 0.23[(a.u.)^2/Hz^{1-\beta}]$,

$\beta = 1$, $\gamma = 4$, and $f_b = 4$ mHz for the bending power law. The values of N are estimated from the relations in table 2 considering $\sigma^2 = 1$. In the following all the spectra are evaluated without zero-padding the time series and imposing the time-halfbandwidth product $NW = 4$ and $K = 7$ tapers.

5.1 Smoothing.

The primary purpose of the smoothing procedure is to reduce the fluctuations of the estimated spectrum around the true value in order to recover the shape of the background spectrum even when high enhancements due to periodic signals occur. Figure 2 show the AR(1) (left), PL (middle), and BPL (right) processes. From the top we report each time series, the *raw* power spectrum (black), the *med* (blue), *mlog* (dashed red), *bin* (green), and *but* (dashed magenta) smoothings, as described in section 4.1, on log-log and semi-log scales. The corresponding smoothing window percentages have been automatically identified via the KS test. Each procedure produces different background fits, primarily due to their different behaviour at the edges of the frequency interval. For example, the *med* smoothing ($p_{KS} = 0.20, 0.20, 0.24$, respectively for the three processes) provides a good representation of the spectrum except at low frequencies where it flattens due to the rapid rise of power toward lower frequencies. It therefore systematically underestimates the true spectrum as evident in the log-log panels (Figure 2d-f). The *mlog* ($p_{KS} = 0.22, 0.19, 0.21$) fit, on the other hand, follow exactly the *raw* spectrum at lower frequencies, but flattens at high frequencies. This approach is particular well-suited for AR(1) processes, that exhibit high variability at low frequencies and flattening toward a white noise spectrum at high frequencies. In contrast, for PL and BPL processes the *mlog* fit overestimates the background spectrum as shown in the corresponding semi-log panels (Figure 2e-f). The *but* ($p_{KS} = 0.03, 0.07, 0.14$ and $n = 18, 13, 13$) approach appears as a smoother version of the *med* with a better representation of the true spectrum at lower frequencies for the PL (Figure 2h) and, especially, for the BPL (Figure 2i) processes. Decreasing the percentage of smoothing, that is increasing the pass band of the low pass filter, the *but* smoothing could give better representation of the low frequency spectrum, but it would rapidly reduce to the *raw* spectrum. Finally, the *bin* approach ($p_{KS} = 0.20, 0.24, 0.19$), known to be an unbiased estimator of the true power spectrum in the case of power law spectrum (Papadakis & Lawrence, 1993), gives a good representation of the background spectrum in all the three cases. Unfortunately, since the cor-

responding frequency range is reduced due to the binning, the values at low and high frequency are extrapolated extending the fitted model to all the frequency range. In any case, unlike the other smoothing procedures, the *bin* approach is unaffected by the spectrum flattening at low frequencies.

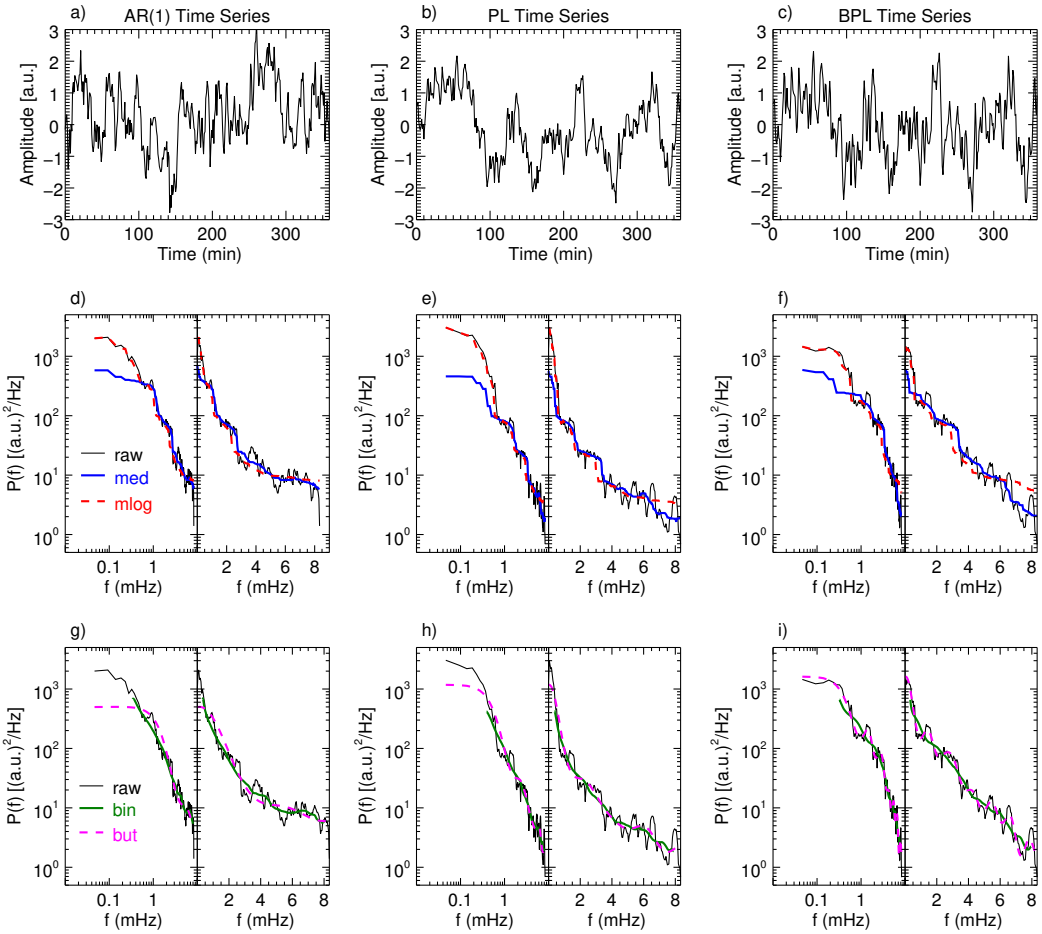

Figure 2. Example of the smoothing procedure for a synthetic representation of AR(1) (left), PL (middle), and BPL (right) processes. Panels a, b, and c show the corresponding time series with unitary variance. Panels d-i show the comparison of the raw spectrum with the smoothed spectra obtained with the *med* (blue), *mlog* (red), *bin* (green), and *but* (magenta) approaches.

5.2 Background Estimate.

Once the *raw* and/or the smoothed spectra have been evaluated, the next step is to fit the smoothed spectra with various models via the maximum likelihood method. Figure 3 shows the background selection procedure for the same time series of Figure

2. For each of the three cases (AR(1), PL and BPL), the background spectra (red lines) are estimated from the raw spectrum and its four different smoothed versions (black lines). The true analytical spectrum is shown by the green dashed lines corresponding respectively to a lag-one autoregressive (Figure 3a), a power law (Figure 3b), and a bending power law (Figure 3c) models using the parameters listed at the top of the panels. All the background spectrum estimation techniques provide a good representation of the true spectrum, but there are some differences. For the AR(1) process, the true spectrum is overestimated at high frequencies and underestimated at low frequencies by all the approaches. In particular, the flattening at low frequencies is clearly visible for the *med*, *bin*, and *but* smoothings (a better representation is given by the same figure in log-log scale provided in the supporting information, Figure S1). For the PL and BPL time series, the raw spectrum shows a flattening at low frequency due to the convolution of the spectral window of the MTM method with the steep true spectrum. Note that this effect strictly depends on the parameters chosen for the MTM analysis; smoothing via the *bin* procedure reduces this effect. For the PL case, the fits tend to underestimate the true values at high frequencies and overestimate at low ones with the exception of the *med* approach, which lies below the true spectrum at all frequencies. For the BPL case, instead, the true spectrum is always underestimated except near the frequency break where it is overestimated. Only the *mlog* approach shows an opposite behaviour due to the excessive flattening of the smoothed spectrum at high frequencies.

In each box we also report the parameters of the estimated background spectrum with their 99% confidence interval, the values of the three choosing criteria (C_{KS}, AIC, and $MERIT$), and the root mean square error ($RMSE$) of the estimate with respect to the true spectrum. The text in red indicates the minimum values of the choosing criteria and $RMSE$ for each panel. In the absence of signals, the best representation of the background spectrum is the one obtained from the *raw* spectrum. In all the scenarios, it minimizes at least one of the three criteria and the $RMSE$ is always among the lowest values. We obtain better representation only for the AR(1) and PL case through the *mlog* approach according to the $RMSE$ values. This result shows clearly that for steep spectra, the low frequency portion plays a fundamental role in the identification of the background model. The *raw* and *mlog* approaches provide a good representation of the low frequency range. Alternatively, this could be achieved with the other methods by

narrowing the smoothing window, but this will result in poor smoothing at higher frequencies, with the smoothed spectrum almost the same as the *raw* spectrum.

The present discussion covers common scenarios for time series frequently observed in space physics environments, but it is not representative of all responses of our methodology. In particular, the most critical regions are the edges of the frequencies intervals. For example, AR(1) time series characterize by low ρ values manifest a flatter trend at low frequencies that can be also be represented well by the *med* and *but* smoothings. In addition, the choice of the analysis parameters such as the time-halfbandwidth product NW, the number of tapers K, degree of zero-padding, and width of the smoothing window might influence the results. Therefore, we always recommend a preliminary investigation on specific sets of measurements to determine the best parameters for a robust spectral analysis.

5.3 Signal Identification.

The last step consists of the identification of periodic signals defined as combinations of power spectrum enhancements with respect to the estimated background spectrum and peaks in the HF test values. Figure 4 shows two examples of an AR(1) with $N = 25.5[(a.u.)^2/Hz]$ and $\rho = 0.90$ with two different sinusoidal signals. Similar results are obtained when using PL or BPL. In Figure 4a, we show the AR(1) noise and three signals (black lines), respectively at $f_1 \approx 1.8$, $f_2 \approx 3.3$, and $f_3 \approx 4.8$ mHz with amplitude $A_1 = 0.30$ and $A_2 = A_3 = 0.15$. Figure 4b shows the raw spectrum (black line), the true spectrum (dashed line), and the AR(1) models obtained from each smoothing approach that is blue for *med*, red for *mlog*, green for *bin*, and magenta for *but*. A smaller box enlarging the 6-8 mHz frequency range shows that, due to the occurrence of power enhancements, the estimated background spectrum tend to be overestimated at high frequencies. Figure 4c shows in the top box the background spectrum based on the *bin* smoothing (green line) selected as the best fit representation of the spectrum according to the *score* defined in section 4.3. The middle box of Figure 4c shows the γ statistic, which is the ratio of the raw and background spectra, while the lower box shows the F statistic. The dashed lines represent the 95% and 99% confidence levels while the three vertical dashed lines identifies the frequencies of the synthetic signals. The power enhancement at ≈ 1.8 mHz is concealed by the background spectrum showing the same order of power density at these frequencies. The signals at ≈ 3.3 and ≈ 4.8 mHz exceed re-

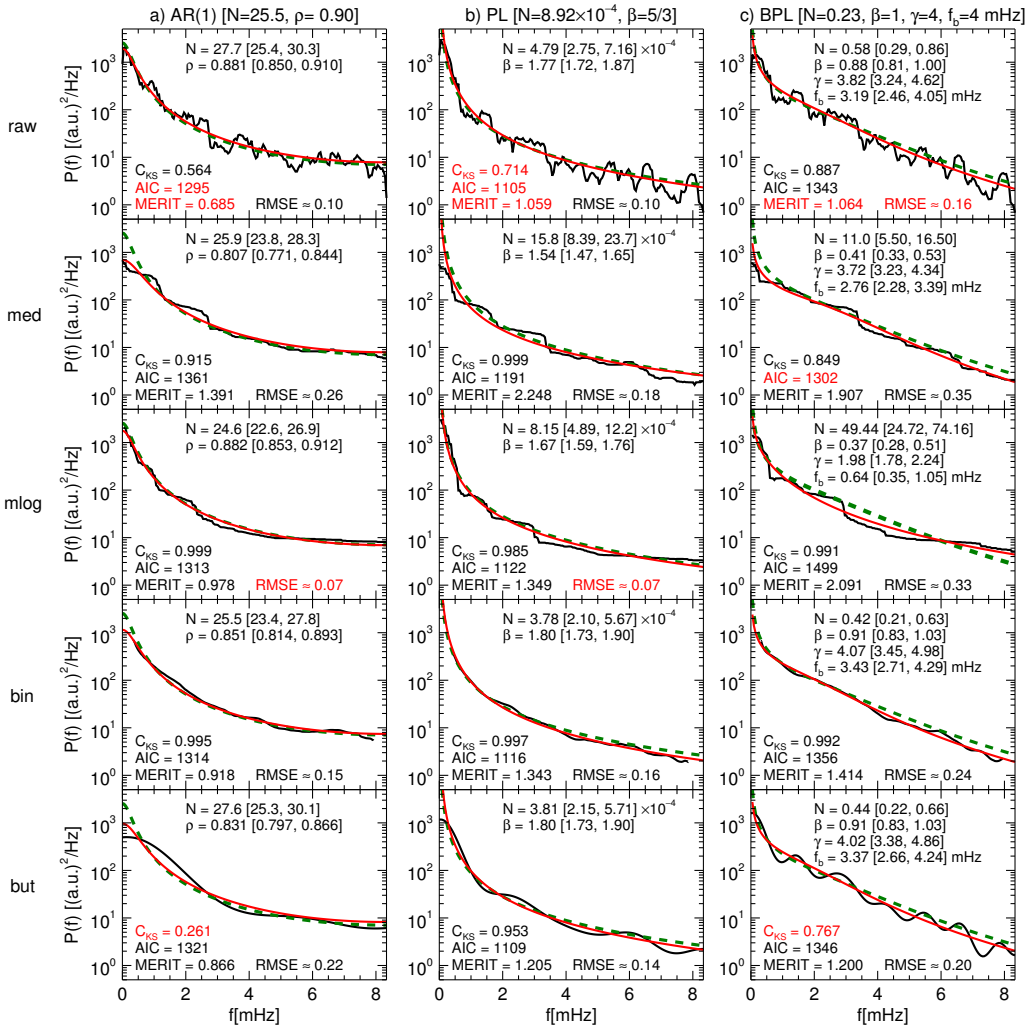

Figure 3. From the top, the black lines represent the direct power spectrum (*raw*) and its four smoothed representations (*med, mlog, bin, but*) for the same AR(1) (column a), PL (column b), and BPL (column c) time series showed in Figure 2. The comparison between the background spectra (red lines), obtained via the maximum likelihood approach, and the true spectra (green dashed lines), whose parameters are given on top of each column, is quantified with their *RMSE*. In each panel, we report the estimated model parameters with the corresponding 99% confidence bounds, together with the values of the selection criteria C_{KS}, *AIC*, and *MERIT*. In each column, the red text highlights the criteria minimum value.

spectively the 95% and the 99% confidence levels. On the other hand, via the HF test the $\approx$ 1.9 mHz signal is identified at the 95% confidence level while the $\approx$ 3.3 and $\approx$ 4.2 mHz exceed the 99% level.

Next, we discuss the special case of multicomponent signals occurring at nearby frequencies within the Rayleigh bandwidth (Di Matteo & Villante, 2017). We add to the time series of the first example signals at nearby frequencies, i.e. $f_1^{'} \approx 1.9$, $f_2^{'} \approx 3.6$, $f_3^{'} \approx 4.2$, and $f_3^{''} \approx 4.4$ mHz with amplitude respectively of $A_1^{'} = 0.30$, $A_2^{'} = A_3^{'} = A_3^{''} = 0.15$. Figure 4d shows the AR(1) noise and the beating of the combined signals (black lines); the resultant time series corresponds to the red line. Figure 4e shows the raw spectrum and the AR(1) models in a similar way as Figure 4b. The smaller box, showing the details of the 6-8 mHz frequency range, indicates how the additional energy of the new signals further enhance the background spectrum estimates at high frequencies. In this case, the background spectrum obtained via the *mlog* approach is selected as the best representation of the true noise spectrum. Figure 4f show the comparison of the raw spectrum with the best AR(1) model, the γ statistic, and the F statistic with vertical dashed lines identifying the signals present in the time series. The frequencies of the signals are at values that are often observed in the solar wind and magnetosphere with frequency separation from below to above the bandwidth of the MTM spectral window ($2B = 2NW/T$), in our simulation $2B \approx 0.4$ mHz. For the signals at ≈1.8 and ≈1.9 mHz, separated by less than ≈0.1 mHz (25% of 2B), we observe a single enhancement both in the γ and in the F statistic passing the 99% confidence level. For the signals at ≈4.2 and ≈4.4 mHz, separated by ≈0.2 mHz (50% of 2B), the power spectrum appears as a broad enhancement at the 95% confidence level, while only a narrow peak with bandwidth less than B pass the 99% confidence level (therefore discarded according to our selection criteria, see section 4.4). Two peaks at the 95% confidence level are selected by the HF test at the right frequency but their values are significant reduced with respect to the ones of other signals at similar amplitude. This result is in agreement with the previous investigations (Di Matteo & Villante, 2017) on the identification rate of synthetic signals at nearby frequencies. At greater separation, for example, ≈3.3 and ≈3.6 mHz corresponding to ≈0.3 mHz (75% of 2B), we still observe a broad enhancement at the 95% confidence level but a separate step-like side lobe corresponding to one of the signals is clearly visible. However, according to our criteria, at least one of the two signals is selected at the 99% confidence level. In the HF test analysis, both the signals are identified at the

99% confidence level. When the frequency separation is equal or greater than the MTM spectral window bandwidth $2B \approx 0.4$ mHz, as is the case for the ≈4.4 and ≈4.8 mHz signals, then there is no mutual effect between the corresponding enhancements in both the γ and F statistic. The level of confidence of the ≈4.8 mHz appear to be same as in the previous example of isolated signals (Figure 4c). Note that the spectrum portions far from the power enhancements remain the same as in the first example, highlighting the robustness of the MTM method against leakage due to monochromatic signals.

6 Examples with Real Observations.

In this section, we show a case study using data taken in the solar wind, magnetosphere and ground observations to demonstrate the performance of our methodology. We consider the periodic fluctuations identified by Viall et al. (2009) in the solar wind proton density and magnetic field measurements at the geostationary orbit on January 15, 1997, extending the analysis onto a longer time interval and to ground observatories. In particular, we show that even though the background spectrum in these three regimes exhibit considerably different shapes, our technique manifests great flexibility and is able to provide good background estimates and identify a common periodicity between all of the spectra.

6.1 Solar Wind.

Periodic variations of the solar wind proton density were observed by the Wind spacecraft on January 15, 1997, between 12:40 and 19:10 UT. We used proton density data derived from the Wind-Solar Wind Experiment (Ogilvie et al., 1995) measurements. The time interval of 6.5 hours, padded with zeros to reach 13 hours, determines a Rayleigh frequency of $f_{Ray} \approx 43$ μHz and a frequency step $\Delta f \approx 21$ μHz, while the average sampling rate of $\Delta t \approx 83$ s corresponds to a Nyquist frequency of $f_{Ny} \approx 6$ mHz. We choose NW=3 and K=4 as parameters for the MTM analysis, therefore the bandwidth for the spectral window is $2B \approx 0.26$ mHz corresponding to the minimum separation needed to distinguish two signals with close frequencies. Figure 5a shows the proton density observations n_p, while Figure 5b shows the corresponding power spectrum, the γ (ratio between the raw and background spectrum) and HF tests. Applying our spectral analysis procedure, we obtained the background power spectrum (red line), via the *mlog* smoothing, as a *PL* with parameters $N \approx 0.024[cm^{-6}/Hz^{1-\beta}]$ and $\beta \approx 1.45$. Then, we tested

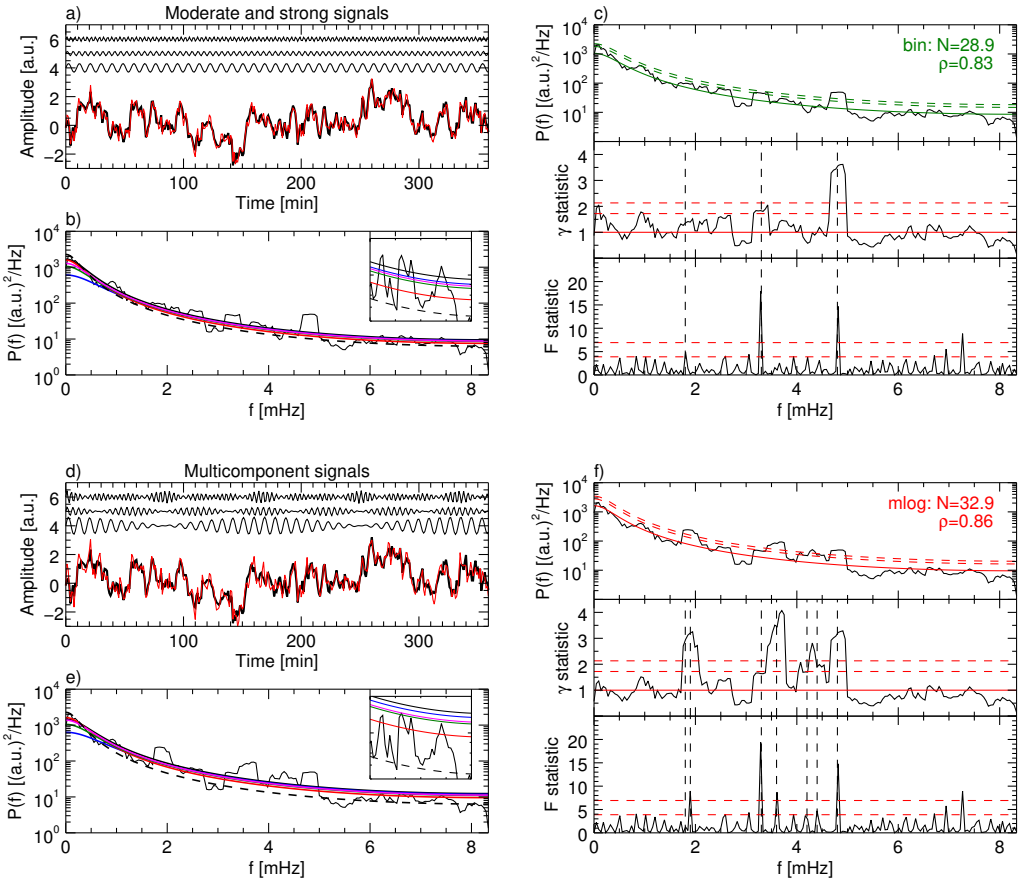

Figure 4. Example of periodicity identification for monochromatic and multicomponent signals. Panels a and d show the analyzed time series (red lines) obtained from the sum of an AR(1) time series (thick black line), with parameters N=25.5 $(a.u.)^2/Hz$ and ρ=0.90, and persistent monochromatic signals (top black lines). Panel b and e, comparison of the *raw* spectrum (black line) with the true spectrum (dashed line) and the AR(1) model spectra fitted on the *raw* (black), *med* (blue), *mlog* (red), *bin* (green), and *but* (magenta) smoothed spectra. Panel c and f, from the top, comparison of the *raw* spectrum with the selected best representation of the background spectrum, their ratio γ, and the HF test. The dashed lines represent the 90% and 95% confidence levels, while the vertical dashed lines identify the frequency of the signals.

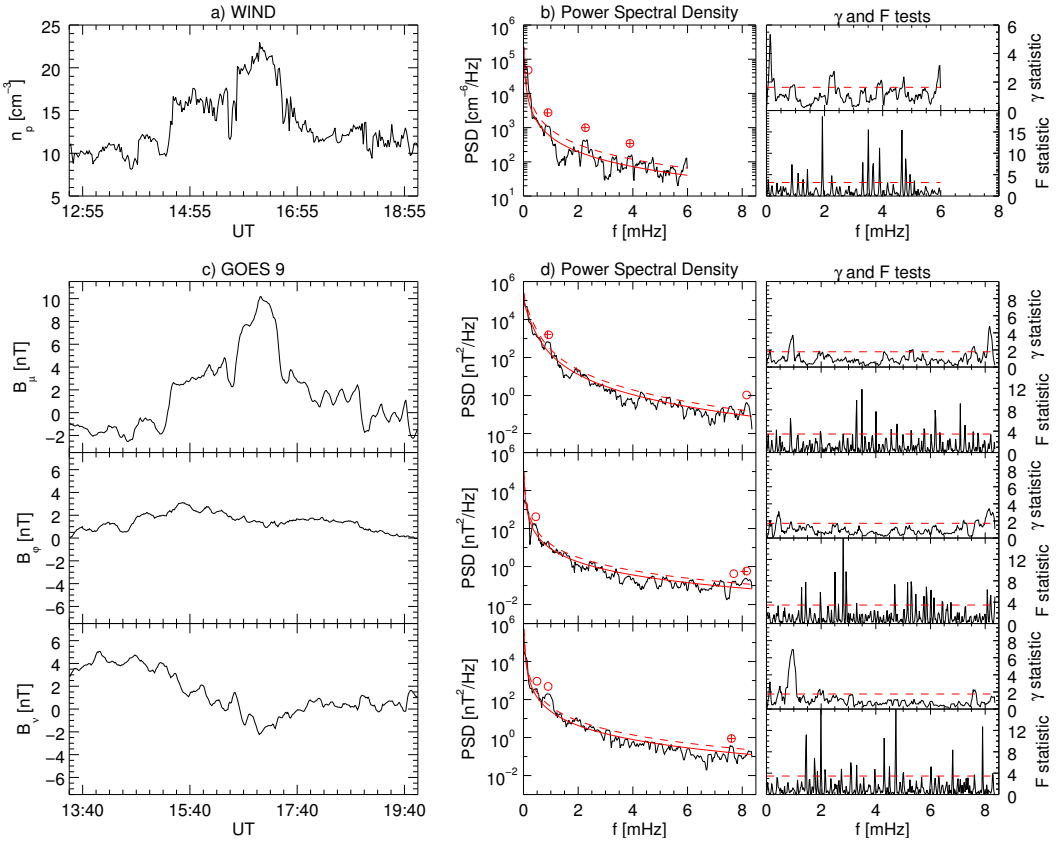

Figure 5. Spectral analysis of the Wind solar wind proton density (top panels) and GOES 9 magnetospheric field components in MFA coordinates (bottom panels) observed on January 15, 1997. From the left, panels a and c show the time series, panels b and d the *raw* power spectral density (black line) compared with the best representation of the background spectrum (red line), their ratio γ and the HF test. The red circles (crosses) identify the frequencies passing the narrow band (narrow band plus HF test) at the 90% confidence level (red dashed lines).

the occurrence of periodic signals at the 90% confidence levels (red dashed lines); we placed circles above the power enhancements passing the narrow band (γ) test adding crosses at the frequencies passing also the HF test in the same frequency range. We identified three clear signals passing both tests at ≈0.88, ≈2.25, and ≈3.89 mHz corresponding respectively to ≈19, ≈7.4, and ≈4.3 min. An additional periodicity at f ≈0.17 mHz (≈100 min) was identified only by the narrow band test. During part of the same time interval analyzed here, Viall et al. (2009), using the M. E. Mann and Lees (1996) approach, identified periodic fluctuations passing both the narrow band and the HF test at $f \approx$ 0.2, ≈ 0.8, and ≈ 2.8 mHz.

6.2 Magnetosphere.

The solar wind described in the previous section was measured near L1, and impacted the magnetosphere after $\approx$ 45 min, corresponding to the time range of 13:25 and 19:55 UT. We investigated the magnetospheric response considering the 60 s (therefore, $f_{Ny} \approx 8.3$ mHz) averaged magnetic field components derived from the triaxial fluxgate magnetic field measurements (Singer et al., 1996) on the GOES 9 geostationary satellite (LT=UT-9) located in the dawn-morning sector (between 4:25 and 10:55 LT). The data have been rotated in the Mean Field Aligned (MFA) coordinate system at each point along the spacecraft trajectory. In MFA coordinates (Takahashi et al., 1990), $\hat{\mu}$ is along the average field, as defined by the N min vector running average; $\hat{\varphi}$ is perpendicular to $\hat{\mu}$ and the spacecraft position vector, positive eastward; $\hat{\nu}$ completes the orthogonal system. To avoid the introduction of spurious periodicity due to the rotation procedure, the average magnetic field is evaluated on a running window of 6.5 hours (Di Matteo & Villante, 2018). Figure 5c shows the three components of the magnetospheric field, while Figure 5d shows the corresponding power spectra, the γ and HF tests. The similarity of the compressive component B_μ with the solar wind density fluctuations is clear, even though the higher frequencies components seems to be filtered out in the magnetosphere at GOES 9 location. Next, we investigate the occurrence and properties of the magnetospheric field fluctuations with our spectral analysis approach. For the compressive component B_μ, we obtained a *raw/BPL* background spectrum with parameters $N \approx 7.60[nT^2/Hz^{1-\beta}]$, $\beta \approx 0.91$, $\gamma \approx 3.54$, and $f_b \approx 0.28$ mHz, while for both the toroidal (B_φ) and poloidal (B_ν) component we found *PL* background spectra respectively combined with a *raw* smoothing, obtaining $N \approx 11.7 \times 10^{-7}[nT^2/Hz^{1-\beta}]$ and $\beta \approx 2.29$, and a *bin* smoothing, obtaining $N \approx 9.0 \times 10^{-7}[nT^2/Hz^{1-\beta}]$ and $\beta \approx 2.48$. At the 90% confidence level (red dashed lines), we identify power spectrum peaks passing the narrow band test at $f \approx$ 8.16 mHz for B_μ, at $f \approx 0.45$ and $f \approx 7.69$ mHz for B_φ, and at $f \approx 0.49$ and $f \approx$ 0.90 mHz for B_ν. In addition, both the γ and HF tests selected signals at $f \approx 0.88$ mHz in B_μ, at $f \approx 8.08$ mHz in B_φ, and at $f \approx 7.60$ mHz in B_ν. Note that the power spectra of both the compressive and poloidal component manifest an enhancement at $f \approx$ 0.9 mHz ($\approx$ 20 min) clearly observed also in the solar wind proton density. In the toroidal and poloidal component, the signals at $f \approx 0.45$ and ≈ 0.49 mHz, corresponding to oscillations of about $\approx$ 37 and $\approx$ 34 min, are mostly related to the first three oscillations observed at the beginning of the time interval ($\approx$ 26, $\approx$ 32, and $\approx$ 36 min). Similar

fluctuations appear also in the solar wind proton density (≈ 26, ≈ 40, and ≈ 36 min), even though there is no clear enhancement in the power spectrum. In fact, other stronger fluctuations at nearby frequencies dominate the low frequency range of the solar wind density power spectrum making it difficult to distinguish additional signals.

6.3 Ground Observatories.

We extended the analysis to ground magnetic field observations from two stations located near the GOES9 magnetic field line footpoint in both latitude and longitude: Yellowknife (YKC, $\lambda = 62.48°$ and $\phi = 245.52°$) and Fort McMurray (FMC, $\lambda = 56.66°$ and $\phi = 248.79°$), where λ and ϕ are the geographic latitude and longitude, respectively. For these examples, we used the 60 s data from the SuperMAG collaboration providing the three components of the magnetic field in the NEZ coordinate system where B_N and B_E are directed toward the locally magnetic north and east, respectively, and B_Z is vertically down. We analyzed the B_N component after the removal of the daily variations and yearly trend determined by the Gjerloev (2012) algorithm. Figure 6a shows the magnetic field observations from the two stations, while Figure 6b shows the corresponding power spectra, the γ and HF tests. Applying our procedure, we obtain as background spectrum a *raw/BPL* with $N \approx 0.06[nT^2/Hz^{1-\beta}]$, $\beta \approx 1.76$, $\gamma \approx 9.51$, and $f_b \approx 6.67$ mHz at YKC, and a *raw/PL* with $N \approx 0.02[nT^2/Hz^{1-\beta}]$ and $\beta \approx 1.56$ at FMC. As in the previous section, we classified the signals identified at the 90% confidence level. We observed four power spectrum peaks at YKC, one passing only the narrow band test at $f \approx 7.90$ mHz and three at $f \approx 0.86$, ≈ 4.92, and ≈ 5.18 mHz passing both the γ and the HF test. The spectral analysis at FMC identified two signals satisfying both the γ and the HF test at $f \approx 0.88$ and $f \approx 6.04$ mHz. The two ground observatories clearly observed the same $f \approx 0.9$ mHz oscillations identified in the magnetospheric field at geostationary orbit, in turn, driven by the solar wind density fluctuations.

6.4 Additional Remarks.

Viall et al. (2009), using the M. E. Mann and Lees (1996) approach, identified, during part of the same time interval, periodic fluctuations passing both the narrow band and HF test, with the 95% confidence level, at $f \approx 0.2$, ≈ 0.8, and ≈ 2.8 mHz in both the solar wind proton density and B_z magnetospheric field component at the geostationary orbit. We find correspondence with our results at $f \approx 0.17$, ≈ 0.88, and ≈ 2.25

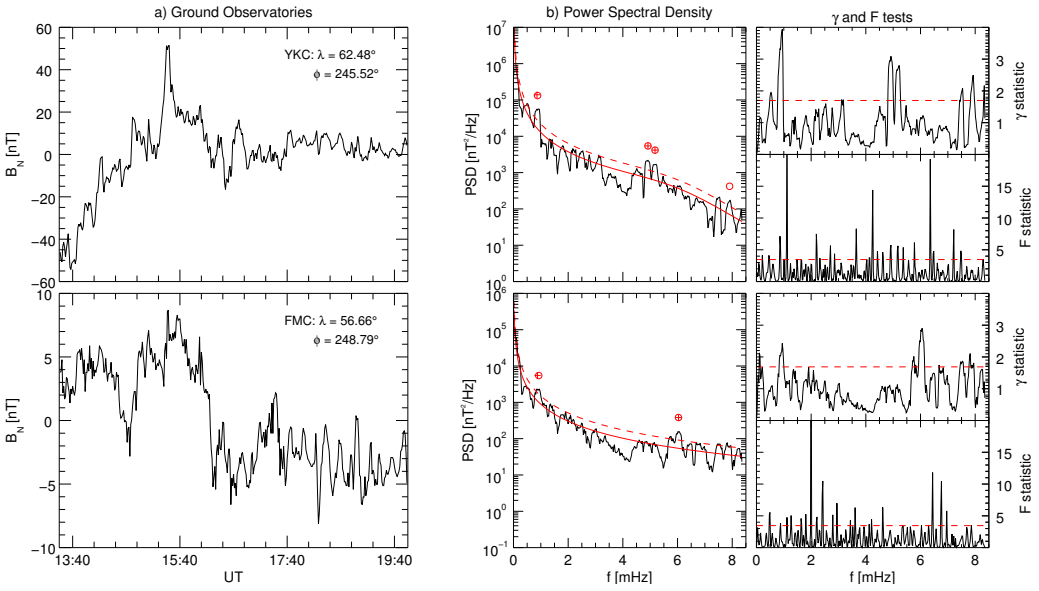

Figure 6. Spectral analysis of the B_N magnetic field component from two ground observatories on January 15, 1997. From the left, panels a show the time series, panels b the *raw* power spectral density (black line) compared with the best representation of the background spectrum (red line), their ratio γ and the HF test. The red circles (crosses) identify the frequencies passing the narrow band (narrow band plus HF test) at the 90% confidence level (red dashed lines).

mHz in the solar wind and at $f \approx 0.9$ mHz at the geostationary orbit and in the two ground observatories. The time series of B_μ at GOES9 show clearly that the longer timescales are directly driven by the solar wind density fluctuations. In addition, paying attention to the low frequency range of the normalized power spectra (γ statistic), we note that three enhancements centered at $f \approx 0.2$, ≈ 0.4, and ≈ 0.9 mHz occur in all the observations, but our procedure is able to automatically identify only the strongest component at $f \approx 0.9$ mHz. The difficulty in the identification of peaks at nearby frequencies and at the edges of the frequency interval are two known limitation of our method. Identification of low frequency signals may be improved by increasing the frequency resolution, that is decreasing $2B$, the width of the spectral window main lobe, either by reducing the NW parameter, or increasing the length of the time interval.

7 Discussion.

We presented a new spectral analysis procedure, based on the MTM method, for the robust modeling of the background spectrum and identification of signals at discrete frequencies. One major challenge in analysis of the power spectra of space physics time series is the wide range of variations observed in them. The adaptive multitaper was specifically introduced by Thomson (1982) to investigate colored power spectra when common spectral analysis techniques might suffer from strong energy leakage, especially for short time series. We use the statistical properties of the adaptive multitaper method to develop a maximum likelihood determination of the background spectra. In addition, extending the M. E. Mann and Lees (1996) approach, we combine different smoothings methods (*raw*, *med*, *mlog*, *bin*, and *but*) and models (*WHT*, *PL*, *AR(1)*, *BPL*) representative of the power spectra usually obtained from space physics time series. This is also reflected by the choice of the parameters range reported in table 2, constrained to represent red power spectra. Finally, objective criteria select the best representation of the background spectrum as well as power spectrum and F values enhancements at defined confidence levels.

We discuss the critical issues in the identification of the background spectrum, for each step of our procedure, with respect to three synthetic time series representing a lag-one autoregressive, a power law, and a bending power law process. The first step, the smoothing of the estimated adaptive multitaper spectrum, is used as a first estimate of the shape of the background spectrum when large enhancements due to geophysical pe-

riodic signals are present. We can perform the smoothing via four different approaches, each of which has its own advantages and disadvantages for fitting red spectra. The *med* approach systematically underestimate steep spectrum at low frequency on an interval comparable to the width of the running window. However, it might give a better representation of the background when strong clear peaks occur at very low frequency. The *mlog* approach, instead, reproduces the raw spectrum at low frequency, while at high frequencies, due to the running window covering a large portion of the frequency interval, returns almost constant values. This behaviour is optimal for a AR(1) process, whose spectrum flattens at high frequency, but determines an overestimation of the background spectrum for power law processes, critical for very steep spectra. The *but* approach provides results similar to the *med* one with better estimates in the low frequency range. The *bin* approach define the smoothed spectrum on a limited range of frequency, therefore the background spectrum at the edge of the frequency interval is extrapolated. However, this procedure provides good representation of the background spectrum in all the three case, especially for power law processes.

When we fit the different models to the smoothed spectra, we obtain a good representation of the true spectrum in most of the smoothing+model combinations. In the absence of a signal, the use of the *raw* spectrum ensures good results in all of the scenarios, as expected. In the examples with synthetic time series, we show that for steep spectra, especially for power law process, the low frequency portion plays a fundamental role in the identification of a reliable background model. This is mainly a concern for short time series that might have few points in the low frequency range. For bending power laws, additional complications might arise when the frequency break is too close to the edges of the frequency interval or when the two spectral indices have close values; in these scenarios the BPL will collapse into a PL. Therefore, a necessary condition for the BPL is to have enough points in each of the two frequency intervals that exhibit different spectral slopes. Both problems might be resolved by considering time series long enough to ensure adequate coverage for both regimes of the power spectrum. When there is a lack of information about the properties of the background model, our technique allows for the smoothing+model combinations to be calculated and the best representation selected according to objective statistical criteria. This is particularly helpful when power enhancements due to periodic fluctuations are present.

As we demonstrated with the synthetic example, the background model is systematically overestimated when the time series consists of a stochastic process and periodic signals. This is due to the additional amount of energy that the periodicity introduces. When such signals are present, a preliminary analysis to find the right combinations of smoothing and model to be probed should be performed. The systematic overestimation of the background spectrum results in a lowering of the confidence levels of the power enhancements relative to the artificially higher background. A similar situation occurs when two periodicities have frequency separation comparable to the width of MTM spectra window main lobe, that is $\Delta f \approx 2B = 2NW/T$. In our examples we discuss different scenarios:

1. $\Delta f \approx 25\%$ of 2B, only one power enhancement present, and the HF test identifies only one of the two signals;
2. $\Delta f \approx 50\%$ of 2B, broad band power enhancement combined with two peaks in the HF test at the correct frequencies, both at a significant reduced confidence level;
3. $\Delta f \approx 75\%$ of 2B, highly confident broad enhancement with a separate step-like side lobe, corresponding to one of the signals, at a lower confidence level, both confirmed in the HF test;
4. $\Delta f \approx$ 2B, power enhancements and HF test peaks are resolved separately.

Note that this classification is for reference only, as in the analysis of real signals, with more complicated spectra, the situation can be more complex (e.g. more than two signals at nearby frequencies).

We demonstrated the techniques by applying them to observations of solar wind proton density, magnetospheric field at geostationary orbit, and ground stations at different latitudes. We analyzed a previously studied time interval during which the solar wind density directly drove compressional fluctuations in the magnetospheric field at geostationary orbit and the magnetic northward component at ground observatories (Viall et al., 2009). The best background representations identified by our procedure corresponded to a power law (for n_p at Wind; B_φ and B_ν at GOES 9; B_N at FMC) and bending power law models (for B_μ at GOES 9; B_N at YKC); in this event study, AR(1) was not found to be the best fit background model for any of the data. This demonstrates the necessity of utilizing different models for a correct evaluation of the background spectrum, es-

pecially in case like the YKC observatory where only the BPL provided reasonable results.

We note that if the goal of the spectral analysis is to identify the nature of the background spectrum and there are no discrete periodicities present, or only weak ones, then our procedure performs best with the background model fitted to the raw spectrum, and no smoothing is performed.

8 Conclusions.

We have developed an automated method for identifying both the background power spectrum and power enhancements in the spectra of time series. We start with the adaptive multitaper method, a sophisticated non-parametric spectral analysis tool suitable for the analysis of colored spectra. A priori knowledge of the statistical properties of the power spectral density allows a robust maximum likelihood fitting of models on the estimated spectrum and the definition of confidence levels. Combining the raw spectrum and its four smoothed representations with four models, the best representation of the background spectrum is selected via robust statistical criteria. Lastly, confident thresholds are used to determime statistically significant discrete power enhancements and, when combined with a harmonic analysis, robustly identifies the frequency of the periodic oscillations occurring in the time series.

The analysis of synthetic time series demonstrates how different combination of smoothings and models influence the determination of the background spectrum, and hence the confidence levels of the power enhancements. In addition, different scenarios on the identification of signals at nearby frequencies show that our method, primary designed to identify isolated monochromatic signals, is still able to distinguish two signals separated by a frequency interval down to half the width of the spectral window main lobe.

The inherent flexibility of our method was demonstrated by the analysis of real measurements in different environments. The analysis of solar wind density and magnetospheric fields observations at geostationary orbit and ground show that the PL and BPL models, combined with the smoothing procedure in occurrence of power enhancements, give the best representation of the background spectra for this event study and frequency range. In addition, the identification of power enhancements at the 90% confidence level in both amplitude and F-tests in our example shows that low frequency magnetospheric

field fluctuations are directly driven by solar wind density oscillations clearly at $f \approx 0.9$ mHz and possibly at $f \approx 0.2$ and ≈ 0.4 mHz. This is in agreement with previously published results (e.g. Viall et al., 2009; Kepko et al., 2002; Kepko & Spence, 2003; Villante et al., 2007).

The approach developed here is applicable to a broad range of research fields that have a need to distinguish between continuous power spectrum and discrete power enhancements. Such applications range from analyzing time-series for statistically significant periodicities to robustly characterizing the spectral background of geophysical systems. Our procedure can fit a given model to provide a robust estimate of the model parameters and their uncertainties. In the case that the user is interested in the nature of the background model, the raw spectrum itself should first provide a reasonable representation of the continuous spectrum associated with the process generating the time series. The modular structure of our methodology allows the introduction of new smoothing methods and models to cover additional types of time series. The flexibility and extensibility of the technique makes it broadly suitable to any discipline.

Generally speaking, this technique provide a good representation of the background spectrum thanks to the different smoothing+model pairs covering more scenarios than previous spectral analysis methods. When combined with an independent harmonic analysis, this allows the robust identification of power enhancements related to coherent persistent monochromatic fluctuations occurring in the time series.

Acknowledgments

The solar wind observations from Wind and the GOES magnetic field data are available at the NASAs CDAWeb site (`http://cdaweb.gsfc.nasa.gov/istp_public/`). Ground observations rely on data collected at magnetic observatories and are available at `http://supermag.jhuapl.edu`. We thank the National Institutes that support them and INTERMAGNET for promoting high standards of magnetic observatory practice (`https://www.intermagnet.org`). The work of S.D., N.M.V., and L.K. was supported under the National Aeronautics and Space Administration Heliophysics Internal Science Funding Model program. Code is available on the Zenodo platform at `https://zenodo.org/***` **the url will be available after publication** (Di Matteo et al., 2020).

References

Akaike, H. (1973). *Information theory and an extension of the maximum likelihood principle.* (B. N. Petrov & F. Csáki, Eds.). Budapest: Akademiai Kiado.

Anderson, E. R., Duvall, T. L. J., & Jefferies, S. M. (1990). Modeling of solar oscillation power spectra. *Astrophysical Journal*, *364*, 699-705. doi: 10.1086/169452

Bevington, P. R., & Robinson, D. K. (2003). *Data reduction and error analysis for the physical sciences* (3rd ed.). Boston, MA: McGraw-Hill. doi: 1969drea.book....B

Bruno, R., & Carbone, V. (2013). The Solar Wind as a Turbulence Laboratory. *Living Reviews in Solar Physics*, *10*(1), 2. doi: 10.12942/lrsp-2013-2

Burnham, K. P., & Anderson, D. R. (2004). Multimodel inference: Understanding aic and bic in model selection. *Sociological Methods & Research*, *33*(2), 261-304. doi: 10.1177/0049124104268644

Cash, W. (1976). Generation of Confidence Intervals for Model Parameters in X-ray Astronomy. *Astronomy & Astrophysics*, *52*, 307. doi: 1976A&A....52..307C

Cash, W. (1979). Parameter estimation in astronomy through application of the likelihood ratio. *The Astrophysical Journal*, *228*, 939-947. doi: 10.1086/156922

Claudepierre, S. G., Mann, I. R., Takahashi, K., Fennell, J. F., Hudson, M. K., Blake, J. B., ... Wygant, J. R. (2013). Van allen probes observation of localized drift resonance between poloidal mode ultra-low frequency waves and 60 kev electrons. *Geophysical Research Letters*, *40*(17), 4491-4497. doi: 10.1002/grl.50901

Cramér, H. (1940). On the theory of stationary random processes. *Annals of Mathematics*, *41*(1), 215–230. doi: 10.2307/1968827

Cramér, H. (1992). On harmonic analysis in certain functional spaces. In S. Kotz & N. L. Johnson (Eds.), *Breakthroughs in statistics: Foundations and basic theory* (pp. 179–184). New York, NY: Springer New York. doi: 10.1007/978-1-4612-0919-5_12

DeForest, C. E., Howard, R. A., Velli, M., Viall, N., & Vourlidas, A. (2018). The highly structured outer solar corona. *The Astrophysical Journal*, *862*(1), 18. doi: 10.3847/1538-4357/aac8e3

Di Matteo, S., Viall, N. M., & Kepko, L. (2020). *SPD_MTM: a spectral analysis tool for the SPEDAS framework.* Retrieved from `https://zenodo.org/***` doi: ***

Di Matteo, S., Viall, N. M., Kepko, L., Wallace, S., Arge, C. N., & MacNeice, P. (2019). Helios observations of quasiperiodic density structures in the slow solar wind at 0.3, 0.4, and 0.6 au. *Journal of Geophysical Research: Space Physics*, *124*(2), 837-860. doi: 10.1029/2018JA026182

Di Matteo, S., & Villante, U. (2017). The identification of solar wind waves at discrete frequencies and the role of the spectral analysis techniques. *Journal of Geophysical Research: Space Physics*, *122*(5), 4905-4920. doi: 10.1002/2017JA023936

Di Matteo, S., & Villante, U. (2018). The identification of waves at discrete frequencies at the geostationary orbit: The role of the data analysis techniques and the comparison with solar wind observations. *Journal of Geophysical Research: Space Physics*, *123*(3), 1953-1968. doi: 10.1002/2017JA024922

Ghil, M., Allen, M. R., Dettinger, M. D., Ide, K., Kondrashov, D., Mann, M. E., ... Yiou, P. (2002). Advanced spectral methods for climatic time series. *Reviews of Geophysics*, *40*(1), 3-1-3-41. doi: 10.1029/2000RG000092

Gjerloev, J. W. (2012). The supermag data processing technique. *Journal of Geophysical Research: Space Physics*, *117*(A9). doi: 10.1029/2012JA017683

Inglis, A. R., Ireland, J., Dennis, B. R., Hayes, L., & Gallagher, P. (2016). A large-scale search for evidence of quasi-periodic pulsations in solar flares. *The Astrophysical Journal*, *833*(2), 284. doi: 10.3847/1538-4357/833/2/284

Inglis, A. R., Ireland, J., & Dominique, M. (2015). Quasi-periodic pulsations in solar and stellar flares: re-evaluating their nature in the context of power-law flare fourier spectra. *The Astrophysical Journal*, *798*(2), 108. doi: 10.1088/0004-637x/798/2/108

Kantz, H., & Schreiber, T. (2003). *Nonlinear time series analysis* (2nd ed.). Cambridge: Cambridge University Press. doi: 10.1017/CBO9780511755798.020

Kepko, L., & Spence, H. E. (2003). Observations of discrete, global magnetospheric oscillations directly driven by solar wind density variations. *Journal of Geophysical Research: Space Physics*, *108*(A6). doi: 10.1029/2002JA009676

Kepko, L., Spence, H. E., & Singer, H. J. (2002). Ulf waves in the solar wind as di-

rect drivers of magnetospheric pulsations. *Geophysical Research Letters*, *29*(8), 39-1-39-4. doi: 10.1029/2001GL014405

Kepko, L., Viall, N. M., Antiochos, S. K., Lepri, S. T., Kasper, J. C., & Weberg, M. (2016). Implications of l1 observations for slow solar wind formation by solar reconnection. *Geophysical Research Letters*, *43*(9), 4089-4097. doi: 10.1002/2016GL068607

Kolmogorov, A. (1941). The Local Structure of Turbulence in Incompressible Viscous Fluid for Very Large Reynolds' Numbers. *Akademiia Nauk SSSR Doklady*, *30*, 301-305.

Koopmans, L. H. (1974). *The spectral analysis of time series*. doi: 1974sats.book....K

Lampton, M., Margon, B., & Bowyer, S. (1976). Parameter estimation in X-ray astronomy. *The Astrophysical Journal*, *208*, 177-190. doi: 10.1086/154592

Mann, I. R., Lee, E. A., Claudepierre, S. G., Fennell, J. F., Degeling, A., Rae, I. J., ... Honary, F. (2013). Discovery of the action of a geophysical synchrotron in the earths van allen radiation belts. *Nature Communications*, *4*(2795). doi: 10.1038/ncomms3795

Mann, M. E., & Lees, J. M. (1996). Robust estimation of background noise and signal detection in climatic time series. *Climatic Change*, *33*(3), 409–445. doi: 10.1007/BF00142586

McHardy, I. M., Papadakis, I. E., Uttley, P., Page, M. J., & Mason, K. O. (2004). Combined long and short time-scale X-ray variability of NGC 4051 with RXTE and XMMNewton. *Monthly Notices of the Royal Astronomical Society*, *348*(3), 783-801. doi: 10.1111/j.1365-2966.2004.07376.x

Murphy, K. R., Inglis, A. R., Sibeck, D. G., Rae, I. J., Watt, C. E. J., Silveira, M., ... Nakamura, R. (2018). Determining the mode, frequency, and azimuthal wave number of ulf waves during a hss and moderate geomagnetic storm. *Journal of Geophysical Research: Space Physics*, *123*(8), 6457-6477. doi: 10.1029/2017JA024877

Nakariakov, V. M., & Melnikov, V. F. (2009). Quasi-periodic pulsations in solar flares. *Space Science Reviews*, *149*(1), 119–151. doi: 10.1007/s11214-009-9536-3

Nita, G. M., Fleishman, G. D., Gary, D. E., Marin, W., & Boone, K. (2014). Fitting

fft-derived spectra: theory, tool, and application to solar radio spike decomposition. *The Astrophysical Journal*, *789*(2), 152. doi: 10.1088/0004-637x/789/2/152

Ogilvie, K. W., Chornay, D. J., Fritzenreiter, R. J., Hunsaker, F., Keller, J., Lobell, J., ... Gergin, E. (1995). Swe, a comprehensive plasma instrument for the wind spacecraft. *Space Science Reviews*, *71*(1), 55–77. doi: 10.1007/BF00751326

Ozeke, L. G., Mann, I. R., Turner, D. L., Murphy, K. R., Degeling, A. W., Rae, I. J., & Milling, D. K. (2014). Modeling cross l shell impacts of magnetopause shadowing and ulf wave radial diffusion in the van allen belts. *Geophysical Research Letters*, *41*(19), 6556-6562. doi: 10.1002/2014GL060787

Papadakis, I. E., & Lawrence, A. (1993). Improved methods for power spectrum modelling of red noise. *Monthly Notices of the Royal Astronomical Society*, *261*(3), 612-624. doi: 10.1093/mnras/261.3.612

Percival, D. B., & Walden, A. T. (1993). *Spectral analysis for physical applications.* Cambridge, UK: Cambridge University Press. doi: 1993sapa.book.....P

Press, W. H., Teukolsky, S. A., Vetterling, W. T., & Flannery, B. P. (2007). *Numerical recipes in C: the art of scientific computing* (3rd ed.). New York, NY, USA: Cambridge University Press.

Protassov, R., van Dyk, D. A., Connors, A., Kashyap, V. L., & Siemiginowska, A. (2002). Statistics, handle with care: Detecting multiple model components with the likelihood ratio test. *The Astrophysical Journal*, *571*(1), 545-559. doi: 10.1086/339856

Rouillard, A. P., Sheeley, N. R., Cooper, T. J., Davies, J. A., Lavraud, B., Kilpua, E. K. J., ... Sauvaud, J.-A. (2011). The solar origin of small interplanetary transients. *The Astrophysical Journal*, *734*(1), 7. doi: 10.1088/0004-637x/734/1/7

Samson, J. C. (1983). Pure states, polarized waves, and principal components in the spectra of multiple, geophysical time-series. *Geophysical Journal International*, *72*(3), 647-664. doi: 10.1111/j.1365-246X.1983.tb02825.x

Sanchez-Diaz, E., Rouillard, A. P., Davies, J. A., Lavraud, B., Pinto, R. F., & Kilpua, E. (2017). The temporal and spatial scales of density structures released in the slow solar wind during solar activity maximum. *The Astrophys-*

ical Journal, *851*(1), 32. doi: 10.3847/1538-4357/aa98e2

Sheeley, N. R., Wang, Y.-M., Hawley, S. H., Brueckner, G. E., Dere, K. P., Howard, R. A., ... Biesecker, D. A. (1997). Measurements of flow speeds in the corona between 2 and 30 $r_{\odot}$. *The Astrophysical Journal*, *484*(1), 472–478. doi: 10.1086/304338

Silverman, B. W. (1986). *Density estimation for statistics and data analysis*. London: Chapman & Hall.

Singer, H., Matheson, L., Grubb, R., Newman, A., & Bouwer, D. (1996). Monitoring space weather with the GOES magnetometers. In E. R. Washwell (Ed.), *Goes-8 and beyond* (Vol. 2812, pp. 299 – 308). SPIE. doi: 10.1117/12.254077

Slepian, D. (1978). Prolate spheroidal wave functions, fourier analysis, and uncertainty v: the discrete case. *The Bell System Technical Journal*, *57*(5), 1371-1430. doi: 10.1002/j.1538-7305.1978.tb02104.x

Stella, L., Arlandi, E., Tagliaferri, G., & Israel, G. L. (1994). Continuum power spectrum components in x-ray sources: detailed modeling and search for coherent periodicities. *Milano Series in Astrophysics*, *Proceeding in International Conference on Applications of Time Series Analysis in Astronomy and Meteorology*(136), 10. doi: arXiv:astro-ph/9411050

Takahashi, K., McEntire, R. W., Lui, A. T. Y., , & Potemra, T. A. (1990). Ion flux oscillations associated with a radially polarized transverse pc 5 magnetic pulsation. *Journal of Geophysical Research: Space Physics*, *95*(A4), 3717-3731. doi: 10.1029/JA095iA04p03717

Thomson, D. J. (1982). Spectrum estimation and harmonic analysis. *Proceedings of the IEEE*, *70*(9), 1055-1096. doi: 10.1109/PROC.1982.12433

Thomson, D. J., & Haley, C. L. (2014). Spacing and shape of random peaks in non-parametric spectrum estimates. *Proceedings of the Royal Society A: Mathematical, Physical and Engineering Sciences*, *470*(2167), 20140101. doi: 10.1098/rspa.2014.0101

Timmer, J., & Koenig, M. (1995). On generating power law noise. *Astronomy & Astrophysics*, *300*, 707. doi: 1995A&A...300..707T

Tsurutani, B. T., Lakhina, G. S., Sen, A., Hellinger, P., Glassmeier, K.-H., & Mannucci, A. J. (2018). A review of alfvnic turbulence in high-speed solar wind streams: Hints from cometary plasma turbulence. *Journal of Geophysical*

Research: Space Physics, *123*(4), 2458-2492. doi: 10.1002/2017JA024203

Tu, C. Y., & Marsch, E. (1995). Magnetohydrodynamic Structures Waves and Turbulence in the Solar Wind - Observations and Theories. *Space Science Reviews*, *73*(1-2), 1-210. doi: 10.1007/BF00748891

Vaughan, S. (2005). A simple test for periodic signals in red noise. *Astronomy & Astrophysics*, *431*(1), 391-403. doi: 10.1051/0004-6361:20041453

Vaughan, S. (2010). A bayesian test for periodic signals in red noise. *Monthly Notices of the Royal Astronomical Society*, *402*(1), 307-320. doi: 10.1111/j.1365-2966.2009.15868.x

Vaughan, S., Bailey, R. J., & Smith, D. G. (2011). Detecting cycles in stratigraphic data: Spectral analysis in the presence of red noise. *Paleoceanography*, *26*(4), PA4211. doi: 10.1029/2011PA002195

Vellante, M., & Villante, U. (1984). Maximum entropy spectral analysis of artificial sinusoidal signals. *Journal of Geophysical Research: Space Physics*, *89*(A1), 351-356. doi: 10.1029/JA089iA01p00351

Viall, N. M., Kepko, L., & Spence, H. E. (2008). Inherent length-scales of periodic solar wind number density structures. *Journal of Geophysical Research: Space Physics*, *113*(A7). doi: 10.1029/2007JA012881

Viall, N. M., Kepko, L., & Spence, H. E. (2009). Relative occurrence rates and connection of discrete frequency oscillations in the solar wind density and dayside magnetosphere. *Journal of Geophysical Research: Space Physics*, *114*(A1). doi: 10.1029/2008JA013334

Viall, N. M., Spence, H. E., Vourlidas, A., & Howard, R. (2010). Examining periodic solar-wind density structures observed in the secchi heliospheric imagers. *Solar Physics*, *267*(1), 175–202. doi: 10.1007/s11207-010-9633-1

Viall, N. M., & Vourlidas, A. (2015). Periodic density structures and the origin of the slow solar wind. *The Astrophysical Journal*, *807*(2), 176. doi: 10.1088/0004-637x/807/2/176

Villante, U., Francia, P., Vellante, M., Di Giuseppe, P., Nubile, A., & Piersanti, M. (2007). Long-period oscillations at discrete frequencies: A comparative analysis of ground, magnetospheric, and interplanetary observations. *Journal of Geophysical Research: Space Physics*, *112*(A4). doi: 10.1029/2006JA011896

Wang, Y.-M., Sheeley Jr., N. R., Socker, D. G., Howard, R. A., & Rich, N. B.

(2000). The dynamical nature of coronal streamers. *Journal of Geophysical Research: Space Physics*, *105*(A11), 25133-25142. doi: 10.1029/2000JA000149

Welch, P. (1967). The use of fast fourier transform for the estimation of power spectra: A method based on time averaging over short, modified periodograms. *IEEE Transactions on Audio and Electroacoustics*, *15*(2), 70-73. doi: 10.1109/TAU.1967.1161901

Zong, Q.-G., Zhou, X.-Z., Li, X., Song, P., Fu, S. Y., Baker, D. N., ... Rme, H. (2007). Ultralow frequency modulation of energetic particles in the dayside magnetosphere. *Geophysical Research Letters*, *34*(12). doi: 10.1029/2007GL029915